The Influence of Nucleus Mechanics in Modelling Adhesion-independent Cell Migration in Structured and Confined Environments

*Studies in Applied Mathematics*

WILEY

STUDIES IN APPLIED MATHEMATICS

ORIGINAL ARTICLE OPEN ACCESS

# A Mathematical Model for Neuron Reorientation and Axonal Growth on a Cyclically Stretched Substrate

Annachiara Colombi | Andrea Battaglia | Chiara Giverso

Department of Mathematical Sciences (DISMA) Politecnico di Torino, DISMA, Torino, Italy

**Correspondence:** Annachiara Colombi (annachiara.colombi@polito.it)

**Received:** 23 December 2024 | **Revised:** 7 August 2025 | **Accepted:** 18 August 2025

**Funding:** The authors wish to thank Giulio Lucci and Roberto Marchello for their support in developing the numerical code for the simulations. GC and AC are members of the Gruppo Nazionale di Fisica Matematica, Istituto Nazionale di Alta Matematica (GNFM-INdAM). This work has been supported by the National Plan for Complementary Investments to the NRRP, project "$D^3$4H—Digital Driven Diagnostics, prognostics and therapeutics for sustainable Health care" [project code PNC0000001, CUP B53C22006100001], Spoke 4, funded by Italian Ministry of University and Research, and European Union—NextGeneration EU. AC has been also supported by the Research Project Prin2022 of National Relevance [project code P2022KHFNB, CUP E53D23017990001] granted by Italian Ministry of University and Research, and the European Union—Next Generation EU.

**Keywords:** growth cone reorientation | neuron cell reorientation | neuron cyclic stretching | tubulin-driven growth | viscoelastic model

## ABSTRACT

Experiments have shown that mechanical cues play a central role in determining the direction and rate of axonal growth. In particular, neurons seeded on planar substrates undergoing periodic stretching have been shown to reorient and reach a stable equilibrium orientation corresponding to angles within the interval $[60°, 90°]$ with respect to the main stretching direction. In this work, we present a new model that considers both the reorientation and growth of neurons in response to cyclic stretching. Specifically, a linear viscoelastic model for the growth cone reorientation with the addition of a stochastic term is merged with a moving-boundary model for tubulin-driven neurite growth to simulate the axonal pathfinding process. Various combinations of stretching frequencies and strain amplitudes have been tested by numerical simulation of the proposed model. The simulations show that neurons tend to reorient toward an equilibrium angle that falls in the experimentally observed range. Moreover, the model captures the relation between the stretching condition and the speed of reorientation. Indeed, numerical results show that neurons tend to reorient faster as the frequency and amplitude of oscillation increase.

**2020 MSC:** 35Q92, 92-10, 92C17

## 1 | Introduction

Neurons are the fundamental units of the nervous system and due to their unique morphology and ability to communicate with other excitable cells, they are among the most complex cells in the animal kingdom. A mature neuron is made up of three main parts (see Figure 1A): a *soma*, *dendrites*, and an *axon*. The soma, also called the *cell body*, is the central part of the neuron that contains the nucleus and most of the cellular organelles. Dendrites are short, branching structures

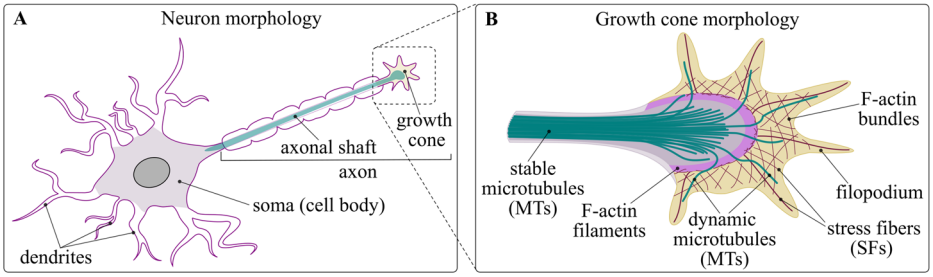


**FIGURE 1** | Schematic representation of the neuron. (A) Neuron morphology during first stage of neuron network development. (B) Internal structure of the growth cone.

surrounding the soma that receive signals from nearby cells. The axon is a long and thin structure that connects the soma to other neurons or tissues, transmitting electrochemical signals.

During neurogenesis, once the soma is fully formed, the neuron begins to sprout small projections known as *neurites*. These neurites will mature into dendrites and an axon, ultimately generating the neural network. A key process necessary to establish the neuronal network is the growth and elongation of the axon from the soma toward a target neuron or another tissue cell. Axonal elongation typically occurs in two consecutive phases. The first, often referred to in the literature as *axon guidance* or *pathfinding*, is here denoted as *tip growth* to emphasize that the elongation is driven by the localized activity at the distal end of the axon. This terminology, although more commonly used for the growth of other biological systems [1], such as angiogenesis, fungal hyphae and plant cells growth, is also adopted in some neuroscience works (e.g., [2, 3]), to highlight the analogy with other contexts in which elongation is guided by dynamic remodeling at the leading edge. The second phase, known as *stretch growth* or *towed axon* phase (first theorized by Weiss in 1941 [4, 5] and then experimentally confirmed [6, 7]) is characterized by elongation resulting from mechanical tension along the axonal shaft. For a comprehensive discussion of stretch growth, see [8]. In this work, we will focus on the better understood tip-growth phase only. During this first phase, the axon growth is guided by a highly motile structure at the axon tip, named the growth cone (GC), which has a very dense cytoskeletal structure (see Figure 1B). The peripheral domain of the GC consists of finger-like filopodia made of F-actin bundles, also known as *stress fibers* (SFs), aligned toward the direction of motion. In the central part of the GC, there is a transitional zone made of actomyosin contractile structures which form a sort of arcs perpendicular to the F-actin filaments. Finally, the rear part of the GC contains all the microtubules (MTs) that enter the GC from the axonal shaft.

The GC plays an important role during the tip-growth phase, as it is able to translate a large variety of stimuli—such as chemotropic molecules, electric signals, mechanical triggers, substrate topography, and stiffness—into directional movement toward the target cell. Once the GC has identified the preferred direction of growth, the GC advancement pulls the axon and the tension generated on it leads to a complex cytoskeletal remodeling process and to the axonal elongation in the GC's preferred direction. This phenomenon, first demonstrated by Lamoureux and colleagues in 1989 [9], was well elucidated by O'Toole et al. [3], who highlighted the combined role of traction forces, viscosity, and adhesions in governing axonal outgrowth. During this phase, the new cellular material, mainly tubulin, is added at the axon tip, in accordance with the classical distal accretion model [2, 10]. However, we acknowledge that recent work [3, 11, 12] suggests alternative or complementary mechanisms in which growth is mediated by intercalation along the axon shaft, driven by tension generated at the GC (see the comprehensive review in [13]). While these perspectives are not explicitly captured in our current formulation, they offer promising avenues for future model extensions.

Finally, once the GC reaches the target cell, it loses most of its motility by transitioning into a series of branched terminations, each one ending with a synapse [10, 14, 15]. The axon is thus established and the synaptic connection is created.

These phases and the development of the nervous system as a whole have traditionally been studied in the context of biochemistry, molecular biology, and genetics. However, there is a growing recognition of the importance of mechanical information in shaping the evolution and development of the neuronal network. Indeed neurons, both in the central and peripheral nervous systems, undergo constant mechanical loading during their lifecycle and are exposed to cyclic strain due to various physiological processes, such as tissue perfusion and movements.

For what concerns the axonal reorientation phenomenon, it is known that the distribution of forces plays a fundamental role in the remodeling process of GC's cytoskeleton, leading to the axon changing its growing direction [10]. Indeed, biological investigations have shown that neurons actively regulate tension along the axon to maintain a rest value and have provide insights into how neurons maintain structural integrity under mechanical load [16]. The effects of

cyclic mechanical stimuli on neurons have been explored in some biological studies, though this area remains under-investigated. Higgins et al. [17] were among the first to study how periodic stretching can promote neurite growth, stimulating human neuroblastoma cells with cyclic uniaxial stretch and observing enhanced neurite growth. Ishibashi et al. [18] similarly demonstrated that dorsal root ganglion neurons showed increased neurite extension when subjected to cyclic stretch, with the extent of growth influenced by the duration of stretching. More detailed studies, such as those by Haq et al. [19], have investigated the combined effects of strain rate and frequency on neuronal development. Specifically, they found that high strain levels led to neurites orienting away from the direction of applied strain, while other conditions resulted in more uniform axon growth. High-frequency stretching appeared to accelerate the reorientation process without significantly altering the final orientation angle. Lin et al. [20] explored the effects of cyclic stretching on neuron reorientation and axonal growth, culturing neurons on a polydimethylsiloxane (PDMS) substrate subjected to cyclic stretching with varying amplitudes and frequencies. Their experimental results showed that neurons tend to reorient their neurites to align "nearly perpendicular", i.e., within the range of $[60°, 90°]$, relative to the direction of the applied cyclic stretch, particularly at higher strain amplitudes. Additionally, the rate of axonal growth was influenced by the cyclic stretch, with higher strain amplitudes leading to faster reorientation and elongation of neurites. The frequency of cyclic stretching had a less pronounced effect compared to the strain amplitude, at least for the range of frequencies tested, suggesting that strain amplitude plays a more crucial role in axonal orientation than frequency, a finding that contrasts with observations in other cell types where frequency is a stronger determinant of reorientation [21].

Over the years, some mathematical models have been developed to understand the underlying mechanisms responsible for neurite and axon elongation and possibly reorientation (see [13] for a comprehensive review). These models can be broadly classified into two main categories, reflecting the underlying biological hypotheses concerning the mechanism of axonal growth. This conceptual distinction reflects the debate between two competing biological hypotheses: the classical view of tip-based elongation via distal accretion of material, and the alternative view of tension-driven intercalation along the axon shaft. The first category includes accretion- and transport-based models, which describe axonal growth as the result of material addition at the distal tip, driven by the supply and polymerization of structural proteins (primarily tubulin) at the GC. These models emphasize the roles of active transport, diffusion, and local assembly dynamics. For instance, compartmental models such as those by Graham and Van Ooyen [22] and their subsequent refinements [23–26] consider the soma and the GC as separate compartments, with growth driven by tubulin concentration at the tip. The second category consists of mechanical models, which treat axons as active viscoelastic or morphoelastic structures whose elongation is regulated by mechanical feedback, cytoskeletal tension, and adhesion forces. The first attempts at modeling the mechanical behavior of axons were made by Dennerll et al. [7], who proposed a simple visco-elastic model, defined by the Kelvin form of the standard linear solid material, to link the axon growth rate to axon tension. This model was later expanded [3] to include the adhesion between the axon and the substrate, through a continuum formulation, in which the neurite under tension interacts with the substrate via frictional forces. Other notable examples that describe growth as a response to internal force generation and external mechanical cues include the active gel models developed by Recho et al. [11], as well as the rod-based frameworks proposed by Oliveri et al. [27–29]. Specifically, a theoretical framework to understand the phenomenon of durotaxis, where axons grow and navigate in response to gradients in substrate stiffness, was initially presented in [27] and recently extended in a comprehensive multiscale model [28], offering insights into the mechanical underpinnings of axonal guidance. Moreover, the mathematical study of how axons, modeled as an active one-dimensional structures, balance external mechanical forces and internal cellular remodeling during growth has been addressed in [29], where a coarse-grained continuum rheological model was derived by homogenizing the internal structure of the cytoskeleton. Finally, a detailed continuum mechanical model, where the axon is treated as a two-phase structure composed of a growing inner core (the axoplasm) and an actively contractile outer layer (the cortical membrane), was proposed by García-Grajales et al. [30]. The model captures the interplay between internal cytoskeletal dynamics, active contraction, and external loading, and predicts distinct mechanical states such as growth, stall, and collapse under different force regimes.

Despite these extensive modeling efforts, the effect of cyclic stretch on neuron reorientation has received relatively little attention. The theoretical framework proposed by Lin et al. [20] remains one of the few models addressing neuron elongation under dynamic stretch. This model connects neuron orientation evolution to the microscopic dynamics of subcellular structures such as SFs, focal adhesions (FAs), and MTs, and it successfully reproduces experimental observations of neuron behavior under cyclic stretching conditions. Furthermore, the mathematical modeling of neurons orientations, despite addressed for other types of cells [21, 31, 32], is still under investigations.

The aim of this study is therefore to introduce a new model for neuron reorientation and growth in response to cyclic stretching. This model simulates the tip growth phase and axon guidance in response to dynamic mechanical stimuli. The soma is assumed fixed and the GC's motion described by an ordinary differential equation (ODE), taking into account the elongation speed and the reorientation process. The evolution of the GC orientation is described by a stochastic differential

equation that combines a linear viscoelastic model, originally developed for other cell types [32] and here adapted for neuron dynamics, with angular fluctuations, described through a Wiener process. The axon tip speed is conversely derived from a diffusion tubulin-driven model for axonal growth [25].

Specifically, in Section 2, the mathematical model for axonal pathfinding and elongation in response to the cyclic stretch of the underlying substrate is presented. Section 3 discusses the numerical implementation (utilizing explicit Euler and finite differences schemes) and details parameter settings, simulation conditions, and results, which will be compared to the experimental observations reported in [20]. Finally, Section 4 summarizes the results, assumptions, limitations, and potential future work.

## 2 | Mathematical Model

### 2.1 | Mathematical Model Set-Up

As mentioned in the previous section, the particular experimental set-up used to study cell reorientation phenomena in [20], that we are going to reproduce numerically in our model, consists of a thin strip of PDMS on which neurons are seeded. Most of the observed and quantified neuronal dynamics (i.e., adhesion, reorientation, and elongation) take place in the $x$–$y$ plane, which is also where the deformation is imposed and measured. Moreover, vertical deformations are neither directly measurable nor expected to significantly affect axonal behavior constrained to the substrate plane. Thus, we adopt a plane strain approximation, treating the substrate as a two-dimensional layer in the $x$–$y$ plane and neglecting deformations along the $z$-axis. Indeed, while out-of-plane strains may arise due to material incompressibility, their influence on the in-plane mechanosensing processes modeled here is assumed to be negligible. Considering the range of strain amplitudes experimentally tested [20], we decide to work under the small deformation assumption, so that the geometry and the constitutive properties of the material at each point can be assumed to be unchanged by the deformation. In addition, experimental data are usually reported for cells located at the central portion of the substrate [21], so that the stress and the strain can be assumed homogeneous [20]. The principal directions thus coincide with the axis along which the stretch is applied and the orthogonal one, and the infinitesimal strain tensor can be expressed as

$$\mathbb{E}(t) = \begin{bmatrix} \varepsilon_x(t) & 0 \\ 0 & \varepsilon_y(t) \end{bmatrix}. \tag{1}$$

With the aim of reproducing the response to cyclic stretching and consistently with [20], we set

$$\varepsilon_x(t) = \frac{\varepsilon}{2}(1 - \cos(\omega t)) = \frac{\varepsilon}{2}(1 - \cos(2\pi f t)) \tag{2}$$

where $\varepsilon$ is the maximum strain amplitude, $\omega$ is the angular frequency expressed in rad/s, and $f$ is the frequency expressed in Hz. In general, the strain along the $y$-axis $\varepsilon_y$ can be either controlled externally or freely determined by the mechanical characteristics of the substrate. In both cases, it is useful to introduce the biaxiality ratio $r(t)$ that represents the percentage of contraction in the $y$-direction with respect to the strain applied along the $x$-axis. In this work, it is assumed constant over time, so that the strain along the $y$-axis can be expressed as $\varepsilon_y(t) = -r\varepsilon_x(t)$. Furthermore, by modeling the substrate as linear, elastic, and isotropic [33], and taking into account the experimental setup in which a given periodic deformation is applied to two opposite sides while the others are stress-free, we can relate the biaxiality ratio to the Poisson's ratio of the material assuming $r = \nu$.

During the tip-growth phase, the substrate deformation is transferred to the soma, the dendrites, the axon, and the GC, thanks to the presence of FAs and SFs in the neuron. For simplicity, in this work, we do not explicitly model FAs and the process of force transmission. We rather assume that (i) the deformation of the substrate is completely transferred to the neuron and (ii) the traction forces generated by the presence of the neurons do not mechanically deform the substrate.

The neuron is modeled assuming the soma fixed in space and neglecting dendrites possibly developing from the cell body. The axon is divided into axonal shaft and GC (see Figure 1A). The axonal shaft is identified as the end-to-end segment from the soma to the GC. In the present description, we assume that the axonal shaft assembles and reorganizes at each instant of time $t$ depending on the position of the GC. This assumption, that allows to model only straight axons, may be consistent in many biological conditions. Indeed, experimental observations [7, 16] suggest that neurons can actively regulate axonal tension to maintain a rest state, which may result in shaft straightening. While this behavior has been reported on substrates other than PDMS, its occurrence under cyclic stretch on PDMS remains to be explicitly confirmed. Furthermore, in the experiments by Lin et al. [20], neurons seeded on cyclically stretched PDMS substrates appear aligned,

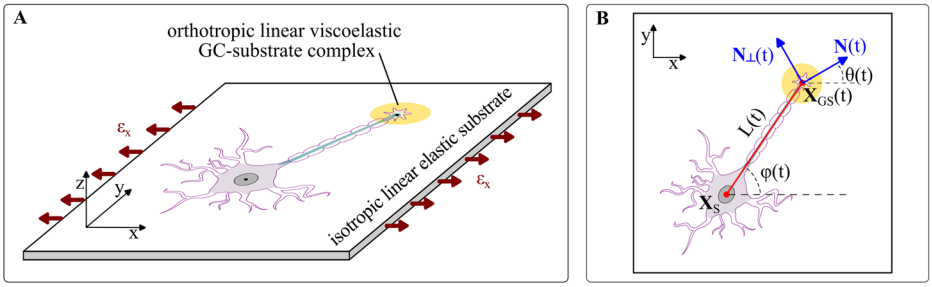


**FIGURE 2** | Representation of the axon–substrate system. (A) The substrate is assumed to behave as a linear isotropic elastic material. The GC–substrate complex (yellow area) has an orthotropic linear viscoelastic behavior. (B) Representation of the neuron in the Lagrangian frame. The positions of the soma and of the growth cone (GC) are $\mathbf{X}_S$ and $\mathbf{X}_{GC}$, respectively. The red solid line represents the axonal shaft. The blue arrow $\mathbf{N}$ is the GC direction of the orientation, defined by the main direction of its stress fibers (SFs). The blue arrow $\mathbf{N}_\perp$ denotes the direction of F-actin bundles connecting the SFs.

although high-resolution imaging of the axonal shaft is not available. We therefore assume a straight axonal shaft in our model, while acknowledging that further experimental evidence is needed to validate this assumption and that in some experimental conditions, such as neuron growth on micro-patterned substrates with specific geometries [19, 34–40], the axons shapes may differ much from a straight lines. Finally, the GC region is modeled as orthotropic and linear viscoelastic as a consequence of the presence of the SFs in the GC and their interaction with the substrate, see Figure 2.

Going into mathematical details, the soma and the GC are represented as material points identified by their positions in the Lagrangian domain, i.e., $\mathbf{X}_S$ and $\mathbf{X}_{GC}(t)$, respectively, see Figure 2B. The axonal shaft thus corresponds to the segment connecting $\mathbf{X}_{GC}(t)$ and $\mathbf{X}_S$, hereafter described by its length $L(t) = \|\mathbf{X}_{GC}(t) - \mathbf{X}_S\|$ and by the angle $\varphi(t)$ it forms with the $x$-axis, i.e., $(\mathbf{X}_{GC}(t) - \mathbf{X}_S) := L(t)\,[\cos\varphi(t), \sin\varphi(t)\,]^T$. The GC is further provided by a direction of orientation $\mathbf{N}(t) = [\cos\theta(t), \sin\theta(t)]^T$, where $\theta(t)$, hereafter named the GC orientation angle, is the angle between $\mathbf{N}$ and the stretch direction $x$. The unitary vector $\mathbf{N}(t)$ denotes the main direction assumed by the SFs constituting the GC cytoskeleton, see Figure 1B, and thus the actual direction of motion of the GC. As observed in Section 1, the SFs in the GC are mutually linked by proteins orthogonally arranged to the fiber bundles, whose direction is $\mathbf{N}_\perp(t) = [-\sin\theta(t), \cos\theta(t)]^T$, that affect the mechanical behavior of the GC.

Axon growth and elongation toward a specific direction during the tip-growth phase is thus here described by the evolution in time of the position of the GC at the axon tip. Having in mind the biological observations reported in Section 1, we assume that

i. the GC direction of motion is dictated by environmental signals, here specifically identified with the substrate deformation (axonal reorientation);
ii. the GC actual displacement requires the addition of new material, i.e., tubulin, to elongate the axonal shaft (axonal elongation).

The dynamics of neuron GC at the axon tip is thus described by the following ODE:

$$\frac{d\mathbf{X}_{GC}(t)}{dt} = V(t)\,\mathbf{N}(t) \tag{3}$$

where $V(t)$ denotes the effective GC speed such that

$$\begin{cases} V(t)\,\cos\theta(t) = \dot{L}(t)\,\cos\varphi(t) - L(t)\,\dot{\varphi}(t)\,\sin\varphi(t), \\ V(t)\,\sin\theta(t) = \dot{L}(t)\,\sin\varphi(t) + L(t)\,\dot{\varphi}(t)\,\cos\varphi(t). \end{cases} \tag{4}$$

Notice that, in the small deflection regime, i.e., when $L\mathbf{N} = \mathbf{X}_{GC} - \mathbf{X}_S + O(\varphi - \theta)$, the GC speed $V$ can be approximated by $\dot{L}$.

As detailed in the following, the axonal reorientation processes determining the evolution of the GC direction of orientation $\mathbf{N}$ is described by the linear viscoelastic model for reorientation proposed in [32], here adapted to the GC pathfinding process with the addition of a stochastic term. This model is further combined with the one-dimensional model proposed in [25] for axonal elongation, that gives the evolution of the axonal shaft length $L(t)$.

## 2.2 | Axonal Reorientation

The axonal reorientation process is here related to the GC response to mechanical stimuli, in particular to cyclic deformations of the substrate. Therefore, the evolution equation for the GC orientation direction $\mathbf{N}$ should account for its dependence on both the frequency and the strain amplitude of the applied substrate deformation. Indeed, in the case of neurons, also the strain amplitude is reported to play an important role in the cell reorientation timing and final angle [20]. With this aim, we follow the approach proposed in [32] by introducing an anisotropic linear viscoelastic model.

As anticipated, the anisotropic behavior of the CG–substratum complex is due to the presence of the SFs in the GC (see Figure 1), and it is thus characterized by SFs' direction of orientation $\mathbf{N}$ and the orthogonal direction $\mathbf{N}_\perp$ along which the binding proteins are placed. Rather, the viscoelastic character is due to the time it takes for the acto–myosin network inside the GC to reorganize and to the continuous rearrangement process of the FAs. Hence, the ensemble of the GC lying on the substrate can be modeled as a Maxwell viscoelastic orthotropic material with a single relaxation time. In the literature, several mathematical models have been developed on the assumption that the equilibrium orientation angle of cells aligns with the direction of minimum strain or minimum stress [41]. However, these models do not accurately capture cell reorientation behavior. In fact, it has been shown that models based on energy minimization provide results that are more consistent with biological evidence [21, 32, 42, 43]. In this regard, following the approach presented in [32], our model assumes that the evolution in time of the GC direction of orientation $\mathbf{N}$, is given in terms of the orientation angle $\theta$ and related to changes in the work $\mathcal{L}$ done by the stress on the GC due to the SFs alignment process. In the linear framework, this work writes $\mathcal{L} := \mathbb{T}(t|\theta) : \mathbb{E}(t)$, where $\mathbb{T}(t|\theta)$ denotes the Cauchy stress tensor given the history of the orientation direction $\theta$, and $\mathbb{E}$ is the infinitesimal strain tensor characterizing the linear terms of the externally imposed deformation. Then, in order to account for the fact that neurons are living entities, each of them possibly reacting in different way to the same stimulus, differently from [32], we include a random term in the model to reproduce the intrinsic randomness in the axonal reorientation process. Therefore, considering an overdamped regime, the following stochastic differential equation for the orientation angle of the GC holds

$$d\theta(t) = -\frac{1}{K\lambda_\theta}\frac{\partial \mathbb{T}}{\partial \theta}(t|\theta) : \mathbb{E}\, dt + \sqrt{\frac{\sigma^2}{\lambda_\theta}}\, dW_t, \tag{5}$$

where $K$ is the Young's modulus of the GC–substrate material, $\lambda_\theta$ is the time the GC needs to reorient itself, $\sigma$ is a parameter representing the stochastic angular fluctuation and $\{W_t\}_{t\geq 0}$ is the standard Weiner process. Considering small enough random fluctuations, the first term on the r.h.s. of Equation (5), which is the same used in [31, 32], implies that the GC tends to assume an equilibrium orientation, said $\theta_{\text{eq}}$, for which the variation of the stress $\mathbb{T}$ with respect to $\theta$ is either null or orthogonal to the deformation given by $\mathbb{E}$. Hence, the product $K\lambda_\theta$ can be seen as a viscous-like coefficient measuring cell resistance to realignment. Furthermore in [32], it was shown that such orientation at the steady state, both in the low- and in the high-frequency regime, is the one leading to the minimization of the elastic energy of the material $\mathcal{U}$ with respect to the orientation angle $\theta$. In (A), such equilibrium orientation are computed for the general orthotropic elastic energy considered in the present work. On the other hand, the second term on the r.h.s. of Equation (5) mathematically represents the variability of cell response to the external stimuli, emerged in experimental observations [20]. Indeed, the equilibrium angle there reported is not unique, but it is given as a range of possible values. Biological evidences thus indicate that, while some general patterns of behavior can be identified, each neuron exhibits a slightly different reaction to the same external mechanical stimulus.

In order to close the model, treating the GC as a Maxwell viscoelastic material, with a single relaxation time $\lambda$, the following evolution equation for $\mathbb{T}$ (see [32] for more details) holds:

$$\lambda\frac{d\mathbb{T}}{dt}(t|\theta) + \mathbb{T}(t|\theta) = \mathbf{C}_0(t|\theta)\frac{d\mathbb{E}}{dt}(t), \tag{6}$$

where the functional $\mathbf{C}_0$ accounts for the exponentially weighted history of past orientations (memory effect), depending on the fourth-order elasticity tensor (or stiffness tensor) $\mathcal{C}_0(\theta(t))$, whose components can be obtained once a proper constitutive orthotropic elastic energy $\mathcal{U}$ is postulated for the mechanical behavior of the GC–substrate complex, through the relation $\mathcal{C}_0^{ijkl} = \partial^2\mathcal{U}/(\partial\mathbb{E}_{ij}\partial\mathbb{E}_{kl})$. The specific form of the orthotropic energy considered in this work is given in Equation (A4) of Appendix A. The functional $\mathbf{C}_0$ is thus defined as

$$\mathbf{C}_0(t|\theta) := \int_{-\infty}^{t} \mathrm{e}^{-(t-\tau)/\lambda}\, \mathcal{C}_0(\theta(\tau))\, d\tau\,. \tag{7}$$

We remark that $\lambda$ refers to the viscous mechanical behavior of the CG–substrate material related to the continuous renewal of adhesion bonds. While, as observed before, $\lambda_\theta$ is related to the time necessary for the cytoskeleton to disassemble and reassemble in order to change the spatial orientation of the SFs and consequently of the GC itself.

### 2.2.1 | Remark: Equilibrium Orientation

As previously discussed, the expression for the equilibrium orientation angle $\theta_{eq}$ can be determined by minimizing the total strain energy stored in the viscoelastic GC with respect to the orientation angle. This leads to an analytical prediction for $\theta_{eq}$, which in turn informs the deterministic part of the reorientation dynamics. The full derivation is detailed in Appendix A. We here report the main results that are useful to understand the behavior of the orientation variable $\theta(t)$ in our model.

Specifically, we assume that the GC–substrate complex behaves as an orthotropic linear elastic material characterized by an elastic energy density $\mathcal{U}$, which depends on the orientation of the SFs. In the small strain regime, this elastic energy is given by:

$$\mathcal{U} = \frac{1}{2}K_{\parallel}(\mathbf{N}\cdot\mathbb{E}\mathbf{N})^2 + 2K_{14}(\mathrm{tr}\,\mathbb{E})(\mathbf{N}\cdot\mathbb{E}\mathbf{N}). \tag{8}$$

where $K_{\parallel}$ is a coefficient related to the stiffness along the SFs direction and $K_{14}$ is a coupling term. Recalling the specific form of $\mathbb{E}$ given by (1)–(2) and neglecting the stochastic term, the minimization of $\mathcal{U}$ with respect to the orientation angle $\theta$ leads to identify three equilibrium GC orientation angles, said $\theta_{eq}$, with values in the interval $[0, \pi/2]$. These angles corresponds to three equilibrium directions $\mathbf{N}_{eq} = (\cos\theta_{eq}, \sin\theta_{eq})$:

- the *parallel equilibrium*, defined by $\theta_{eq} = 0$,
- the *perpendicular equilibrium*, given by $\theta_{eq} = \frac{\pi}{2}$,
- the *oblique equilibrium*, corresponding to values of $\theta_{eq}$ satisfying

$$\cos^2\theta_{eq} = \frac{1}{2}\left(1 - \mathcal{K}\,\frac{1-r}{1+r}\right), \tag{9}$$

being the coefficient

$$\mathcal{K} = \frac{K_{\parallel} + 4K_{14}}{K_{\parallel}} \tag{10}$$

a dimensionless parameter encapsulating the mechanical properties of the GC–substrate complex.

This formulation allows us to prescribe $\theta_{eq}$ in accordance with experimental data by appropriately tuning the value of $\mathcal{K}$. It is important to note that the corresponding angles and directions, can be found in the other quadrants due to symmetry reasons. Finally, we remark that the stability of this equilibrium depends on the dimensionless stiffness ratio $\mathcal{K}$ and on the biaxiality ratio, $r$ (see Appendix A for a comprehensive discussion on the stability).

## 2.3 | Axonal Elongation

The axonal elongation is described with the one-dimensional model proposed in [25, 26] as an extended version of those previously presented in [22, 23]. This model ideally sets the tubulin assembly as the main and only factor responsible for neuron growth, neglecting the potential contribution of mechanical cues in axon elongation. Even though mechanical cues surely play a role in the neuron growth process, experiments reported in [20] did not reveal significant differences in axonal length between neurons subjected to cyclic mechanical loading and control samples. This finding motivated our decision to omit tension-related terms in the axonal growth model. At the same time, the inclusion of a tubulin-based model, even though decoupled from the mechanical framework, allows to mechanistically link the GC speed to biologically relevant processes, such as tubulin synthesis, degradation, polymerization/depolymerization, and steady-state concentration. This formulation thus allows migratory speed to be expressed in terms of biologically meaningful parameters, rather than relying on ad hoc empirical assumptions.

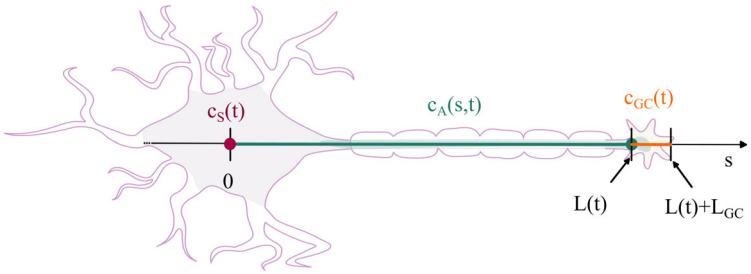


**FIGURE 3** | One-dimensional representation of the axon for the tubulin-driven axon growth model. The tubulin concentration in the soma, $c_S(t)$ and in the growth cone, $c_{GC}(t)$, are assumed to be spatially homogeneous, whereas the tubulin concentration along the axonal shaft, $c_A(s,t)$, is considered a function of the coordinate $s$ along the axon direction.

As stated in Section 1, during the tip-growth phase, axonal elongation is promoted by the assembly of new material (tubulin) in correspondence of the axon tip, to form new MTs. Specifically, in neurons, the tubulin is produced in the soma only, and then transported along the axonal shaft to reach the GC. In the axonal shaft, part of the tubulin is actively transported by motor proteins, while free tubulin diffuses. Another source of tubulin in the GC is the disassembly/depolymerization of MTs required for GC reorientation. In addition, a constant degradation of tubulin occurs in both the axonal shaft and in the GC. The model proposed in [25, 26] accounts for all these processes to describe the temporal evolution of axonal length $L(t)$, depending on the amount of tubulin. Tubulin molecules are small enough to be considered as a continuum and described through their concentration in the different portions of the neuron.

The three main parts of the neuron, i.e., the soma, the axonal shaft, and the GC, are treated as confining regions in a one-dimensional frame aligned to the axon direction, given by the angle $\varphi(t)$, see Figure 3. Letting $s$ denote the coordinate along this direction, the position of the virtually point-like soma $\mathbf{X}_S$ corresponds to $s = 0$. The axonal shaft is mathematically represented by the segment from $s = 0$ to $s = L(t)$, while the GC, located at the tip of the axonal shaft $\mathbf{X}_{GC}(t)$ at $s = L(t)$, is characterized by an assigned characteristic length $L_{GC}$.

The tubulin concentration in the soma, along the axonal shaft, and in the GC are denoted by $c_S(t)$, $c_A(s,t)$, and $c_{GC}(t)$, respectively. Note that the spatial variable $s$ appears only in the axonal shaft, where tubulin transport occurs, while in the soma and GC the tubulin concentration is assumed to be spatially homogeneous. Additionally, $c_A$ represents the concentration of both motor protein-bound and free tubulin.

Then, tubulin produced in the soma is assumed to have the known concentration. The function $c_S(t)$ is thus an input of the model as it defines the amount of tubulin at the beginning of the axon. In the axonal shaft, the active transport of motor protein-bounded tubulin and the free tubulin diffusion are assumed to occur with constant velocity $a$ and diffusion coefficient $D$, respectively. Denoting by $g$ the constant rate of degradation of tubulin, the mass conservation in the axonal shaft leads to the following advection–diffusion–reaction equation:

$$\frac{\partial c_A(t)}{\partial t} + a\frac{\partial c_A(t)}{\partial s} - D\frac{\partial^2 c_A(t)}{\partial s^2} = -g c_A(t) \quad \text{for} \quad 0 < s < L(t). \tag{11}$$

Dealing with a diffusion equation, in the absence of barriers among the neuron regions, we expect the solution $c_A(s,t)$ to be smooth. Hence, it is natural to impose the continuity at $s = 0$ and $s = L(t)$, i.e., to set $c_A(0,t) = c_S(t)$ and $c_A(L(t),t) = c_{GC}(t)$.

To close the model, evolution equations for $c_{GC}(t)$ and $L(t)$ are derived accounting for the processes occurring in the GC (see [25, 26] for a complete deduction of the following equations). A mass balance equation relating the growth of the axonal shaft length to the assembly/disassembly of tubulin to/from MTs occurring in the GC, leads to

$$\frac{dL(t)}{dt} = r_g\left(c_{GC}(t) - c_{GC}^{\infty}\right). \tag{12}$$

where $r_g$ is the rate of length increase, while $c_{GC}^{\infty}$ is the steady-state tubulin concentration at which the assembly and disassembly processes occur at the same rate, resulting in no elongation. The mass conservation of tubulin in the GC compartment conversely leads to

$$\frac{dc_{GC}}{dt} = \frac{1}{L_{GC}}\left(a c_A^- - D\partial_s c_A^- - r_g\left(c_{GC} - c_{GC}^{\infty}\right)c_A^-\right) - g c_{GC} - \tilde{r}_g(c_{GC} - c_{GC}^{\infty}), \tag{13}$$

where $c_A^- := \lim_{s\to L(t)^-} c_A$ and $\partial_s c_A^- := \lim_{s\to L(t)^-} \frac{\partial c_A}{\partial s}$ are, respectively, the concentration of tubulin and its derivative just behind the GC, while $\tilde{r}_g$ is the tubulin polymerization rate consistently proportional to $r_g$ (see again [25, 26]). The first term on the right-hand side of Equation (13) is related to the net flux of tubulin over the fictitious boundary at $s = L(t)$ between the axon and the GC. This term accounts for a net inflow of tubulin into the GC if the tubulin velocity just behind the boundary exceeds the boundary's own speed; otherwise, it results in outflow. Lastly, the second and third terms on the right-hand side of Equation (13) describe, respectively, the constant degradation of tubulin and the assembly/disassembly of tubulin into and from MTs.

#### 2.3.1 | Remark: Equilibrium Length

The convergence of the GC concentration $c_{GC}(t)$ to a steady-state value $c_{GC}^{\infty}$, for the one-dimensional moving-boundary model for axonal growth without reorientation, has been rigorously studied by Diehl et al. [25]. We refer to that publication for a detailed analysis. In particular, it was shown that under biologically realistic parameters and constant soma concentration $c_S$, the system can admits a unique stable steady state. In particular, the GC concentration converges to a critical threshold $c_{GC}^{\infty}$, at which polymerization and depolymerization are balanced, and the elongation rate vanishes. As a result, the axonal length $L(t)$ asymptotically approaches a finite value $L_\infty$, which is determined by the system parameters, including the soma concentration $c_S$, the active transport velocity $a$, the diffusion coefficient $D$, and the degradation rate $g$. On the other hand, the values of the rate constants $r_g$ and $\tilde{r}_g$ have no influence on the steady-state values, but only on the dynamic behavior and convergence to steady state.

## 3 | Results and Discussion

### 3.1 | Numerical Implementation

The mathematical model for axon growth and reorientation, given by Equations (3)–(13), has been numerically solved by discretizing the equations of the model both in time and space.

The total time interval of the simulation $[0, T]$ is partitioned into $N_T$ intervals with fixed time step $\Delta t = T/N_T$. The axon configuration at each time instant $t^n = n\Delta t$, with $n = 0, \dots, N_T$, is approximated by the position of the GC $\mathbf{X}_{GC}^n \approx \mathbf{X}_{GC}(t^n)$ and its orientation angle $\theta^n \approx \theta(t^n)$.

Given the initial conditions $\mathbf{X}_{GC}^0 = \mathbf{X}_{GC}(0)$ and $\theta^0 = \theta(0)$, the explicit Euler scheme approximates Equation (3) as

$$\mathbf{X}_{GC}^{n+1} = \mathbf{X}_{GC}^n + \Delta t\, V^n \mathbf{N}^n, \quad \text{for any } n = 0, \dots, N_T, \tag{14}$$

where $V^n \approx V(t^n)$ and $\mathbf{N}^n = (\cos\theta^n, \sin\theta^n)$ are the GC direction of orientation and the effective GC speed at the time instant $t^n$, respectively. The numerical scheme detailed below first estimates the GC speed $V^n$ by solving system (4), where $\dot{L}$ is provided by the resolution of tubulin-driven axonal elongation model in Section 2.3. The GC orientation angle $\theta^n$, and thus $\mathbf{N}^n$, is then updated by solving the axonal reorientation model in Section 2.2.

For what concerns the axon growth velocity $\dot{L}$, we need to solve the system composed by Equations (11)–(13), which also update the tubulin concentration along the axon $c_A$ and in the GC $c_{GC}$. As a remark, the PDE (11) describes the one-dimensional transport process of tubulin from the soma to the GC, i.e. over a domain with a moving boundary, so that the domain length itself is part of the solution of the system. In order to work on a constant spatial domain, a spatial scaling of the model is performed, following the procedure outlined in [23, 25, 26]. Specifically, the growing domain is rescaled to the constant interval [0,1] by introducing

$$\zeta := \frac{s}{L(t)}, \qquad \frac{\partial \zeta}{\partial s} = \frac{1}{L(t)}, \qquad \frac{\partial \zeta}{\partial t} = -\frac{sL'(t)}{L^2(t)} = -\frac{\zeta L'(t)}{L(t)}, \tag{15}$$

with $s \in [0, L(t)]$ and $\zeta \in [0, 1]$. The tubulin concentration on the $\zeta$-domain is denoted with $c_A(\zeta, t) := c_A(\zeta L(t), t)$, so that

$$\frac{\partial c_A}{\partial t} = \frac{\partial c_A}{\partial t} - \frac{\zeta L'(t)}{L(t)} \frac{\partial c_A}{\partial \zeta}, \qquad \frac{\partial c_A}{\partial s} = \frac{1}{L(t)} \frac{\partial c_A}{\partial \zeta}, \qquad \frac{\partial^2 c_A}{\partial s^2} = \frac{1}{L^2(t)} \frac{\partial^2 c_A}{\partial \zeta^2}. \tag{16}$$

The system in Equations (11)–(13) can be thus rewritten on the fixed domain and there solved. The $\zeta$-interval [0,1] is divided into $M$ computational segments of size $\Delta\zeta = 1/M$. The approximation of the spatial derivatives is made using second-order central finite differences, while for the term $\partial_y c_A^-$ in Equation (13) a one-sided second-order approximation is used. The explicit Euler method is used for the time discretization by adopting the time step $\Delta t$ used for Equations (14)–(20). In order to prevent numerical oscillations and let the method converge to the solution, the discretization parameters $\Delta t$ and $\Delta\zeta$ have to satisfy the following the CFL condition and Cell–Péclet condition, respectively:

$$\Delta t \leq \left( g + \frac{2D}{L_{\min}^2 \Delta\zeta)^2} \right)^{-1}, \qquad \Delta\zeta \leq \frac{2D}{(a + 2r_g c_{\max}) L_{\min}} \tag{17}$$

where $L_{\min}$ is the minimal axon length that can be achieved and $c_{\max}$ is the maximal tubulin concentration (see [25, 26] for further details).

The GC speed $V^n$, as well as the axon reorientation speed $\varphi^{n+1}$, are then obtained from Equation (4). If $\cos(\theta_n - \phi_n) \neq 0$, i.e., if the direction of the GC $N^n$ is not orthogonal to the axonal shaft, we solve the following discretized version of Equation (4):

$$\begin{bmatrix} \Delta t\ \cos(\theta^n) & L^n \sin(\varphi^n) \\ \Delta t\ \sin(\theta^n) & -L^n \cos(\varphi^n) \end{bmatrix} \begin{bmatrix} V^n \\ \varphi^{n+1} \end{bmatrix} = \begin{bmatrix} \dot{L}^n \Delta t\ \cos(\varphi^n) + L^n \varphi^n \sin(\varphi^n) \\ \dot{L}^n \Delta t\ \sin(\varphi^n) - L^n \varphi^n \cos(\varphi^n) \end{bmatrix}. \tag{18}$$

Otherwise, imposing proper geometrical conditions, we have that

$$\begin{cases} \varphi^{n+1} = \varphi^n + \operatorname{acos}(L^n / L^{n+1}) \\ V^n = L^{n+1} \operatorname{sign}(\varphi^{n+1} - \varphi^n)\ \sin(\varphi^{n+1} - \varphi^n)/\Delta t. \end{cases} \tag{19}$$

Lastly, the value of the GC orientation angle $\theta^n$, and thus of $\mathbf{N}^n$, is updated following the procedure presented in [32], for the deterministic term and here adapted to our framework to take into account the stochasticity of the process. Specifically, using a first-order centered finite-difference scheme and considering the components $T_{xx}$ and $T_{yy}$ of $\mathbb{T}$, the discretization of Equation (5) reads

$$\begin{aligned} \theta^{n+1} = \theta^n - \frac{\Delta t}{K\lambda_\theta} \Bigg[ & \frac{T_{xx}^n(\theta + \Delta\theta) - T_{xx}^n(\theta - \Delta\theta)}{2\Delta\theta} \\ & - r \frac{T_{yy}^n(\theta + \Delta\theta) - T_{yy}^n(\theta - \Delta\theta)}{2\Delta\theta} \Bigg] \varepsilon_x^n + \sqrt{\frac{\Delta t\, \sigma^2}{\lambda_\theta}} \xi^n, \end{aligned} \tag{20}$$

where $\xi^n$ is a realization at time instant $t_n$ of the angular fluctuation $\xi \approx \mathcal{N}(0,1)$. The explicit Euler scheme is also used in the approximation of the time derivatives present in the constitutive Equation (6), while the trapezoidal rule has been used to approximate the integral term present in the definition of $\mathbf{C}_0$, given by Equation (7), as outlined in [32].

The whole numerical scheme has been implemented in Matlab. For reader's convenience, in Algorithm 1 all the steps necessary to solve the complete model are listed.

### 3.2 | Parameter Estimation

The parameter values characterizing the mechanical properties of the substrate have been set by referring to the experiments conducted in [20], where a $20 \times 60 \times 1$ mm PDMS strip cured for 2 h at 80°C is used. Considering this specific preparation condition, the material is reported to have Poisson ratio $\nu = 0.495$ [44] and Young's modulus $K = 2.05$ MPa [45]. As said in Section 2, the substrate is cyclically pulled by two lateral clamps, with an imposed strain $\varepsilon_x(t)$ in the form of Equation (2), while the $y$-axis strain is defined by the biaxiality ratio $r = \nu$. In the forthcoming simulations, the stretching amplitude $\varepsilon$ and frequency $f$ are varied within ranges that include the values tested in [20], i.e., $\varepsilon = \{2\%, 5\%, 10\%\}$ and $f = \{0.05, 0.15, 0.25\}$ Hz, respectively. Consistently, in all the forthcoming simulations the period of observation of the system evolution is set to 120 h, i.e., the experimental time period adopted in [20]. Concerning the axonal reorientation model in Section 2.2, it is hard to find in the literature proper experimental data to estimate the

**ALGORITHM 1** | Algorithm to solve the complete model.

**Inputs**:

- axon initial position: $\boldsymbol{X}_{\mathrm{S}}$ and $\boldsymbol{X}_{\mathrm{GC}}^{0}$, as well as $L^{0}$ and $\varphi^{0}$;
- growth cone initial direction: $\theta^{0}$, and thus $\mathbf{N}^{0}$;
- initial tubulin distribution: $\mathbf{c}_{\mathrm{A}}^{0}$, $c_{GC}^{0}$;
- substrate deformation: $\mathbf{C}_{0}(0)$ and $\mathbb{T}(0)$; $f$ and $\varepsilon$.

**Main loop**:

**for** $n = 0, 1, \ldots, N_T$ **do**

1. Compute $\mathbf{c}_{\mathrm{A}}^{n+1}$, $c_{\mathrm{GC}}^{n+1}$, $\dot{L}^{n}$, and so $L^{n+1}$
   by solving the discrete version of Equations (11)-(13)
2. Compute $V^{n}$ and $\varphi^{n+1}$, and so $\dot{\varphi}$
   by solving the discrete version of Equation (4) (i.e., Eqs. (18) and (19))
3. Compute $\mathbf{X}_{\mathrm{GC}}^{n+1}$ using Equation (14)
4. Compute $\mathbf{C}_{0}^{n+1}$ using a discretized version of Equation (7)
5. Compute $\mathbb{T}^{n+1}$ using a discretized version of Equation (6)
6. Compute $\theta^{n+1}$ from Equation (20), and thus $\mathbf{N}^{n+1}$

**end for**

mechanical parameters of the GC–substrate complex involved in the orthotropic energy, given in Equation (8), and thus in Equation (7). These parameters have been therefore estimated by imposing the desired preferential direction of the GC experimentally detected. Indeed, as stated in Section 2.2 and detailed in Appendix A, the value of the oblique equilibrium is characterized by Equation (9). According to biological pieces of evidence presented in [20], neurons tend to reorient themselves primarily along the direction corresponding to angles within the interval $[60°, 90°]$, or the symmetric angles in the other quadrants. Therefore, the oblique equilibrium angle is set to coincide with the average value of the interval $[60°, 90°]$ obtaining $\theta_{\mathrm{eq}} = 75°$, and consequently $\mathcal{K} = 2.56$. Notice that with this values we coherently obtain that only the oblique equilibrium is stable while the other two equilibria are unstable (see Appendix A for further details).

The other parameters appearing in the axonal reorientation model in Section 2.2 are conversely set on the basis of experimental observations or measurements. The GC reorientation time $\lambda_{\theta}$ in Equation (5) and the GC relaxation time $\lambda$ in Equation (5) are respectively set equal to 60 s and 1 s. These values qualitatively reproduce the biological observations reported in [20], as we shall see in Section 3.4, and fall within the biologically admissible range. In fact, the change in the GC direction and the consequent steering of the axon requires a time in the order of minutes, according to [46], while the GC viscous relaxation time has been measured to be below 10 s in [47]. Lastly, the angular dispersion parameter $\sigma$ in Equation (5) is set to 0.0095 on the basis of the variance of the orientation angles reported in [20] for the experiments conducted with $\varepsilon = 10\%$, and the approach adopted in [48].

Regarding the axonal growth model in Section 2.3, the soma is always assumed located at the center of the substrate which is also taken as the center of the reference frame, i.e., $\mathbf{X}_{\mathrm{S}} = (0, 0)\,\mu$m. The initial length of the axonal shaft $L_0 := L(0)$ is supposed comparable to the characteristic length $L_{\mathrm{GC}} = 4\ \mu$m of the GC [25], so that $L_0$ is always set equal to 5 $\mu$m.

The tubulin concentration in the soma is supposed to remain constant in time and equal to twice the steady-state concentration, i.e., $c_{\mathrm{S}}(t) = \bar{c}_{\mathrm{S}} = 2c_{\mathrm{GC}}^{\infty}$ for any $t$, as in [25, 26], since this assures the axonal grow provided that $gL_{\mathrm{GC}} < a$. Since the axon is initially very short, the initial tubulin concentration along the axonal shaft is assumed uniform and equal to the tubulin concentration in the soma, i.e., $c_{\mathrm{A}}(s, 0) = \bar{c}_{\mathrm{S}}$ for any $s \in (0, L_0)$. For the same reason, the initial tubulin concentration in the GC is set equal to the concentration in the soma, i.e., $c_{\mathrm{GC}}(0) = \bar{c}_{\mathrm{S}}$. The estimation of the other parameters in the axonal growth model in Section 2.3 have been done starting from ranges of values indicated in [25, 26], see Table 1, which are considered biologically valid based on experiments conducted on various types of neurons and cells [49–52]. However, the results in [25, 26] show that the nominal values they adopted lead to an excessively rapid growth of the axonal length $L$ compared to the experimental data reported in [20], where a specific neuron lineage, namely PC12 cells, was considered. Therefore, while maintaining the biologically admissible ranges presented in the fourth column of Table 1, the specific values of the growth model parameters (listed in the third column of Table 1) will be selected in Section 3.3.2 to reproduce the growth without stretch as experimentally observed in [20].

**TABLE 1** | Model parameter nominal values and plausible intervals taken from the pertinent literature.

| Parameters | Description | Value | Range | Unit | Ref. |
|---|---|---|---|---|---|
| $\nu$ | Substrate Poisson/biaxiality ratio | 0.495 | | – | [44] |
| $K$ | Substrate Young's modulus | 2.05 | | MPa | [45] |
| $\varepsilon$ | Stretching amplitude | | 1%–30% | — | [20] |
| $f$ | Stretching frequency | | 0.01–1 | Hz | [20] |
| $\mathcal{K}$ | Mechanical behavior of GC-complex | 2.56 | | – | [estim.] |
| $\lambda_\theta$ | GC reorientation time | 60 | | | [46] |
| $\lambda$ | GC relaxation time | 1 | | s | [47] |
| $\sigma$ | Angular dispersion parameter | 0.0095 | | – | [estim.] |
| $a$ | Tubulin active transport speed | 0.005 | 0.005–0.03 | $\mu$m s$^{-1}$ | [25, 26] |
| $D$ | Free tubulin diffusion coefficient | 1 | 1–25 | $\mu$m$^2$ s$^{-1}$ | [25, 26] |
| $g$ | Tubulin degradation rate | $5 \cdot 10^{-7}$ | $10^{-7}$–$200 \cdot 10^{-7}$ | s$^{-1}$ | [25, 26] |
| $L_{GC}$ | GC characteristic length | 4 | 0.1–1000 | $\mu$m | [25, 26] |
| $r_g$ | Microtubules increase length rate | $2.3 \cdot 10^{17}$ | | $\mu$m$^4$ (mol s)$^{-1}$ | [estim.] |
| $\tilde{r_g}$ | Tubulin polymerization rate | 0.05 | | s$^{-1}$ | [25, 26] |
| $c_{GC}^{\infty}$ | Tubulin steady-state concentration | $11.90 \cdot 10^{-21}$ | | mol $\mu$m$^{-3}$ | [25, 26] |
| $c_S$ | Tubulin concentration in the soma | $2c_{GC}^{\infty}$ | 0–$4c_{GC}^{\infty}$ | mol $\mu$m$^{-3}$ | [25, 26] |
| $L_0$ | Initial axonal shaft length | 5 | | $\mu$m | [estim.] |

Abbreviation: GC, growth cone.

### 3.3 | Analysis of the Different Parts of the Model

This section is dedicated to the analysis of the different parts of our model. We begin by exploring the system's behavior when neurons are allowed only to reorient, i.e., solving Equations (5) and (6). Specifically, different values of $\varepsilon$ and $f$ are considered showing how they affect the evolution of the GC orientation, while the equilibrium angle value is properly preserved. Then, we focus on the system's behavior when neurons are allowed only to grow, i.e., by solving Equations (11)–(13) keeping $\mathbf{N}$ fixed in time. Different values of key model parameters are varied by discussing how they influence the axon elongation. A comparison with the biological experiments reported in the literature validates the parameter values in Table 1.

#### 3.3.1 | Reorientation Parameters

To study the response of the model to changes in the parameters related to reorientation model, we first do not consider the growth of the neuron and the motion of the neuron tip, nor the stochastic term. Hence, the dynamics of the orientation angle $\theta$ is solved according to Equations (5) and (6), with $\sigma = 0$. In all the simulations, the starting GC orientation angle is set to $\theta(0) = 30°$ and the substrate is initially undeformed, assuming the stress tensor $\mathbb{T}(0|\theta(0))$ equal to 0. First, the frequency $f$ is fixed at $f = 0.25$ Hz and distinct values of stretching amplitude $\varepsilon$ in the range 1%–30% are considered, see Figure 4A. Then, the stretching amplitude $\varepsilon = 10\%$ is kept constant by testing frequencies in the range 0.011– Hz, see Figure 4B. With the aim to compare our results with those presented in [20], we have included the stretching amplitudes 2%, 5%, and 10% in the simulations with fixed frequency, and the frequencies 0.05, 0.15, and 0.25 Hz in the simulations with fixed amplitude.

Figure 4A highlights that the higher the strain rate is, the faster the reorientation process occurs. Indeed, for $\varepsilon = 30\%$ the equilibrium angle is reached after just 15 h. Conversely, for $\varepsilon = 10\%$ it is necessary to wait around 120 h in order to see the GC reaching the oblique equilibrium $\theta_{eq} = 75°$. For lower values of strain (e.g., $\varepsilon = 5\%$), the reorientation is still in process after 120 h. Instead, for very low values of the strain rate the reorientation process takes much longer times, leading to a barely visible reorientation during the experimental observation time. These numerical results are thus in good agreement with experimental data collected after 24, 72, and 120 h of stretching in [20]. In fact, with a frequency of $f = 0.25$ Hz, neurons showed no significant reorientation when $\varepsilon = 2\%$; whilst at $\varepsilon = 10\%$ a large number of neurons

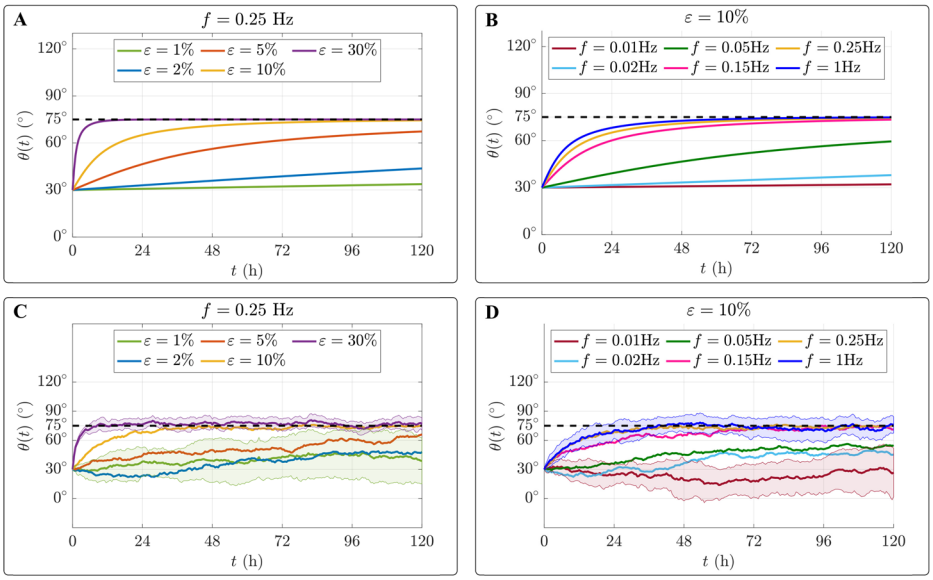


**FIGURE 4** | Time evolution of the growth cone orientation angle $\theta(t)$ obtained by solving Equations (5) and (6), by either assuming $\sigma = 0$ (A and B) or $\sigma = 0.0095$ (C and D). In the latter cases, the solid lines represent the mean evolution of $\theta$ over 100 distinct realizations, colored areas the relative standard deviations. (A and C) The stretching frequency $f$ is fixed at 0.25 Hz, while the amplitude $\varepsilon$ varies. (B and D) The stretching amplitude $\varepsilon$ is fixed at 10% and various frequencies are tested. In all cases, the initial condition is $\theta(0) = 30°$. All the other parameters are always set as in Table 1. In all the simulations, the timestep $\Delta t$ is set to 0.004 s.

aligned themselves to angles between 60° and 90° within just 24 h, and after 120 h all the cells resulted aligned in that direction. The reorientation process was also observed in [20] for $\varepsilon = 5\%$, albeit at a slower rate, resulting in some neurons not aligning to the equilibrium direction.

We now consider the simulations in which the strain rate is fixed at $\varepsilon = 10\%$ and various frequencies $f$ are tested, including also the values used in [20] (i.e., 0.05, 0.15, and 0.25 Hz). Considering the results reported in Figure 4B, it is clear that higher frequencies induce reorientation with a characteristic time that decreases with the frequency. However, the acceleration in the reorientation process saturates above a given threshold. We can indeed notice in Figure 4B that after around 60 h the behavior for the highest frequencies tested (i.e., 0.15, 0.25, and 1 Hz) is substantially the same and the final reorientation angle of the GC is reached after 120 h. The results are consistent with the biological evidence in [20]: considering $f = 0.05$ Hz the reorientation process takes place in a longer time compared to what occurs with higher frequency values as $f = 0.15$ Hz and $f = 0.25$ Hz.

Another interesting phenomenon that can be seen from our simulations is the presence of a minimum threshold under which the cyclic stretch does not induce any significant response in the GC orientation. This happens also with other cell types [32]. In our case, the threshold value can be quantified around $f = 0.017$ Hz. This frequency sets the transition from the low-frequency regime to the high-frequency one. Since we have that $\lambda_\theta \gg \lambda$, the transition is mostly affected by $\lambda_\theta$ and happens when $\lambda_\theta f \approx 1$. In the high-frequency regime, the relaxation time $\lambda_\theta$ is much longer than the oscillation period $T$ of the cyclic deformation. So, the reorganization process of the cell is slower than the period of the imposed strain. The GC response in this case is elastic and it reorients itself by minimizing the energy [32]. On the contrary, in the low-frequency regime, the reorientation process becomes viscous. The period of the imposed deformation is much longer than $\lambda_\theta$ and therefore the GC adapts to the imposed strain, showing an anisotropic viscous-like response. Even though also in the low-frequency regime the steady cell configurations are predicted by a minimization with respect to the orientation angle of the energy introduced in the elastic case [32], this steady configuration is not reached during the time scale of the biological experiment. Indeed, based on our simulations, it is evident that there is no significant reorientation of the GC even after 120 h when the frequency is at 0.01 Hz, which falls under the low-frequency regime. Additionally, we observed that for a frequency of 0.02 Hz, which is only slightly above the minimum threshold, the reorientation process takes longer than the experimental observation period. This result cannot be directly compared to the experimental data in [20], since in that work all the tested frequencies belong to the high-frequency regime, where the GC successfully reorients.

In order to highlight the contribution to the neuron reorientation process due to the stochastic term introduced in Equations (5), for each case considered in Figure 4A,B we performed 100 independent realizations by setting the angular

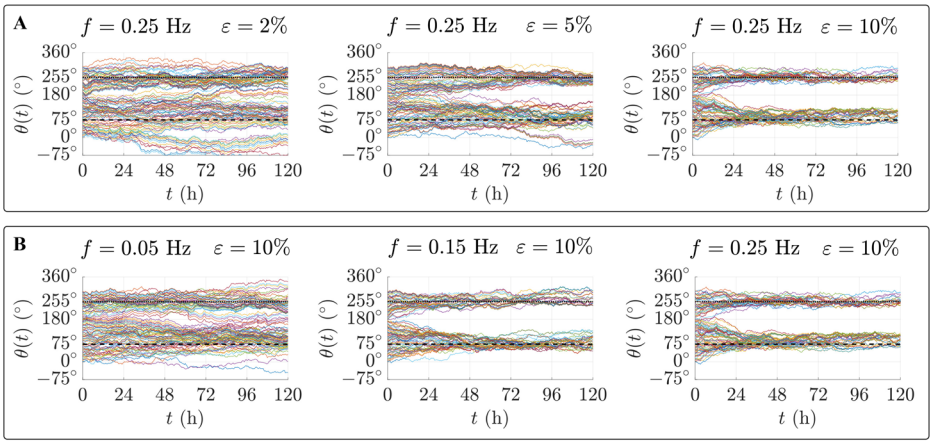


**FIGURE 5** | Time evolution of the growth cone orientation angle $\theta(t)$ obtained by solving Equations (5) and (6) by assuming $\sigma = 0.0095$ and considering 120 different initial values for $\theta(0)$ uniformly distributed over $[0, 2\pi]$. (A) The stretching frequency $f$ is fixed at 0.25 Hz, while the amplitude $\varepsilon$ varies. (B) The stretching amplitude $\varepsilon$ is fixed at 10% and various frequencies are tested.

dispersion parameter $\sigma$ to 0.0095 (as specified in Section 3.2). Solid lines in Figure 4C,D denote the mean value of $\theta(t)$ over the 120 realizations, while colored areas represents the standard deviation. The latter has been reported only for extreme values of $\varepsilon$ or $f$ for graph readability.

As expected, the stochastic term perturbs the convergence of $\theta$ to $\theta_{\text{eq}}$. However, the overall behavior of the system is well preserved. Indeed, as in the case $\sigma = 0$, the GC still rapidly tends to assume values close to $\theta_{eq}$ for sufficiently high strain amplitudes (i.e., $\varepsilon \geq 10\%$ in Figure 4C) or high enough strain frequencies (see $f \geq 0.15$ Hz in Figure 4D). Moreover, it is worth noting that the faster the convergence, the lower the standard deviation of $\theta$. The proposed model therefore successfully captures the typical behavior of cells undergoing random motion in the absence of stimuli strong enough to trigger their polarization.

Lastly, to complete the analysis of this part of the model, we also analyze the evolution of the direction of polarization of the growth cone by considering different initial conditions, see Figure 5. Specifically, for each combination of strain amplitude and frequencies considered in Figure 5, Equations (5) and (6) are solved assuming $\sigma = 0.0095$ and considering 120 different initial values for $\theta(0)$ uniformly distributed over $[0, 2\pi]$. These results highlight that the dynamics observed iFigure 4 do not depend on the specific initial condition. In fact, regardless of the initial value of $\theta(0)$ and the presence of random fluctuations, the GC tends to align with $\theta_{eq}$ (i.e., $\pm 75° + k \cdot 180°$, with $k \in \mathbb{N}$) more rapidly as the strain amplitude or frequency increases.

### 3.3.2 | Axonal Growth Parameters

In this section, we first investigate the behavior of the axonal growth model as key parameters vary. Specifically, we here focus only on the parameters related to the transport mechanism of tubulin along the axon (i.e., active transport $a$ and diffusion $D$). Indeed, within the biologically feasible range reported in the literature for the tubulin degradation rate $g$ (see Table 1), very small changes in axonal length are observed over the period of our interest (simulations not shown). For a more comprehensive analysis of the behavior of the axonal growth model without reorientation, we refer the reader to [25, 26].

We start by varying the tubulin active transport velocity $a$ (see Figure 6A). As expected, the higher the transport of tubulin along the axonal shaft is, the longer the resulting axon will be. This is due to the fact that, with a higher transport velocity, more tubulin reaches the GC from the soma, leading to an increased assembly rate of new MTs. We observe that increasing the values of $a$ results in a longer axonal extension, following an approximately linear trend, at least within the range of values considered. Increasing values of $D$ also result in a longer axonal length (Figure 6B). However, in this case, for lower values of $D$, even a small increase can lead to a significant extension of the axonal shaft, while at higher values of $D$, the rate of axonal growth increment becomes smaller.

Taking into account the behavior of the system for varying parameters, we identified the set of model parameter values listed in the third column of Table 1 that properly fit the experimental data presented in [20] in terms of both axon length

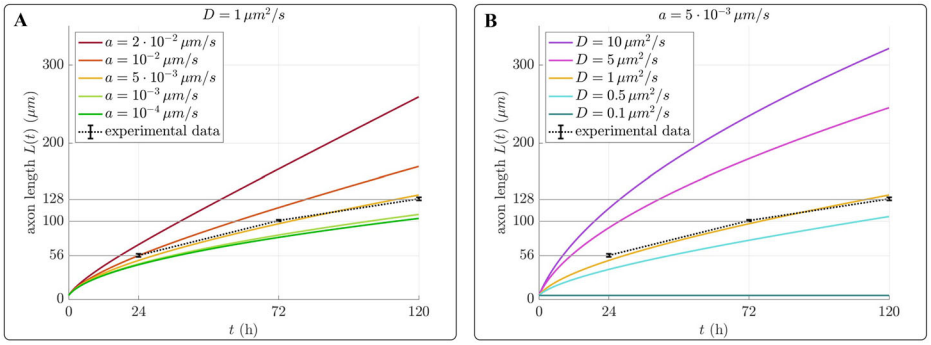


**FIGURE 6** | Variation of the axonal growth as the key parameters $a$ or $D$ vary, while the other parameters are fixed as in Table 1. All the simulations are obtained by solving Equations (11)–(13) with fixed **N**. (A) Axonal length evolution obtained by setting different values of the active transport $a$. The space and timesteps are $\Delta\zeta = 0.02$ and $\Delta t = 0.005$ s. (B) Axonal length evolution obtained by setting different values of the active transport $D$. The space and timestep are $\Delta\zeta = 0.02$ and $\Delta t = 0.0005$ s. The dashed lines denotes the experimental values reported in [20].

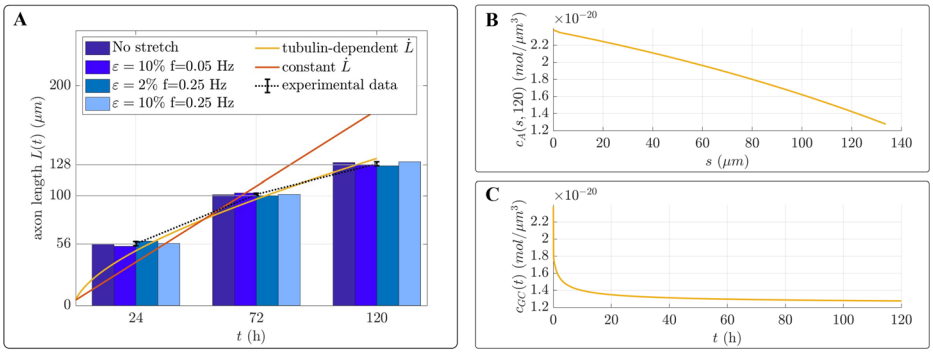


**FIGURE 7** | Numerical results obtained with the nominal values in Table 1 fitting the experimental behavior reported in [20]. All simulations are performed by setting $\Delta\zeta = 0.02$ and $\Delta t = 0.005$ s. (A) Comparison between the numerically obtained axon length $L(t)$ (solid lines) and experimental values in [20] (colored vertical bars). The latter are obtained assuming that $\dot{L}$ is either given by Equation (12) being tubulin-driven (gold solid line); or constantly equal to $4 \cdot 10^{-4} \mu m\,s^{-1}$ (red solid line). The data are reported after 24, 72, and 120 h from the beginning of the experiment. (B) Tubulin concentration profile along the axonal shaft and the growth cone after. (C) Time evolution of the tubulin concentration in the growth cone.

and tubulin concentration, see Figure 7. In particular, Figure 7A shows that the axon length simulated with the proposed parameter setting (gold solid line) qualitatively agrees with the data given by [20] at different times of the axonal elongation process (here reported with the colored vertical bars). In addition, in Figure 7A is also reported the axon length numerically obtained by assuming that the phenomenon of growth occur with constant velocity (brown solid line), i.e., ignoring the tubulin-driven axonal growth model. The velocity considered is $\dot{L} = 4 \cdot 10^{-4}\,\mu m\,s^{-1}$ which is simply an average of the experimental instant velocities reported in [20] at 24, 72, and 120 h. The discrepancy between the brown solid line and the experimental results further validates the assumption that GC speed is accurately captured by the tubulin-driven axonal growth model through Equation (12). Of course, the experimentally observed growth speed could be more simply reproduced by prescribing an explicit time-dependent function. However, such an ad hoc formulation would hardly enable a mechanistic connection between growth speed and biologically relevant processes.

From the simulation with the tubulin-driven growth, we report the tubulin concentration profile along the axon after 120 h, see Figure 7B, and the evolution of the tubulin concentration in the GC, see Figure 7C. In particular, Figure 7B highlights that the maximum value of tubulin concentration is in correspondence of the soma, and it gradually decreases moving toward the GC. At the axon termination, we have the lowest value of concentration corresponding with the tubulin concentration present in the GC. This is consistent with the fact that the flux of tubulin goes from the soma to the axon tip. For what concerns the concentration of tubulin in the GC we can notice how it rapidly decreases form the initial value $c_{GC}(0) = 2c_\infty$ to reach the equilibrium value $c_\infty$ as we expected.

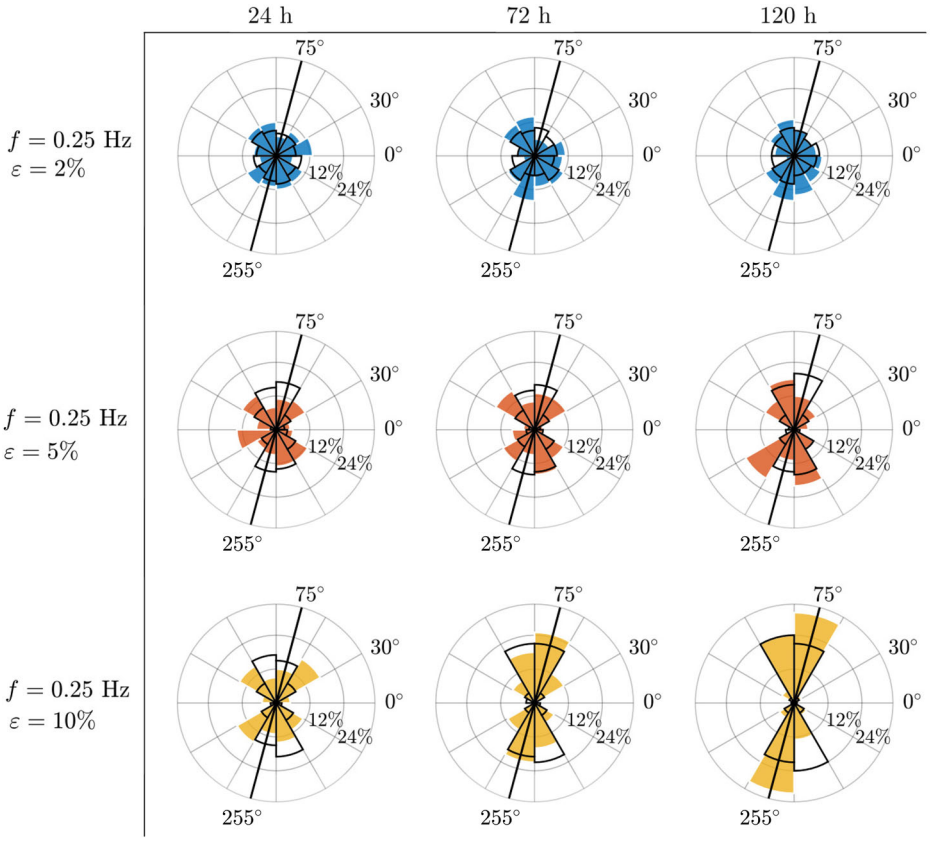


**FIGURE 8** | Simulated neuron reorientation with tubulin-driven axonal growth model and strain frequency $f$ fixed to 0.25 Hz. Different strain amplitudes are considered: $\varepsilon = 2\%$ (top row), $\varepsilon = 5\%$ (central row), $\varepsilon = 10\%$ (bottom row). For each case, 120 neurons initially uniformly distributed over $[0, 2\pi]$ are simulated. Polar histograms show the distribution of their axonal shaft direction $\varphi$ at 24 h (left), 72 h (central), and 120 h (right). In all cases, the circle has been divided into 12 slices measuring 30° each and the percentage of neurons falling into each sector is recorded. As a remark, the equilibrium direction $\theta_{eq} = 75°$ is highlighted. The results of the biological experiments from [20] are shown as black contours to facilitate comparison with the numerical simulations.

### 3.4 | Growth and Reorientation Simulations: Comparison With Biological Experiments

In this section, we compare the prediction of our complete model with the biological experiments proposed in [20]. For each combination of stretching frequency and amplitude there studied, we analyze $N = 120$ numerical realizations of our model, reproducing the growth and reorientation of an individual neuron. In all simulations, the initial direction of the axonal shaft is randomly selected assuming $\varphi(0)$ uniformly distributed in the range $[0°, 360°]$, to faithfully reproduce the random initial orientation of axon. As a remark, the initial direction of the GC is aligned with that of the axonal shaft, i.e., $\theta(0) = \varphi(0)$. First, it is worth to stress that, in the proposed model, the tubulin-driven axonal growth does not directly depends on strain amplitude and frequency. Therefore, keeping all the other model parameters fixed, both the time evolution of axonal length $L$ and tubulin concentrations are always identical to those reported in Figure 7, regardless the values of $f$ and $\varepsilon$. Interestingly, the model successfully reproduces the experimental values taken from [20] and reported in the histogram in Figure 7.

In order to validate our model, the same combinations of stretching frequency and amplitude experimentally tested in [20] are here considered. To easily compare our numerical results to the experimental outcomes in [20] the stretching frequency is first fixed at $f = 0.25$ Hz and distinct values of stretching amplitude $\varepsilon = \{2\%, 5\%, 10\%\}$ are investigated. Then, by fixing the stretching amplitude $\varepsilon = 10\%$, the stretching frequency is respectively assumed equal to $f = \{0.05, 0.15, 0.25\}$ Hz. For each scenario, in Figure 8 and 9, the distribution of the axon orientation $\varphi(t)$ and the corresponding experimental data from [20] obtained at 24, 72, and 120 h, are represented in circular histograms as in the original paper of Lin et al. [20]. We remark that in our mathematical description, the orientation angle of the GC, $\theta(t)$, and the orientation of the axon, $\varphi(t)$, may generally differ. This is consistent with biological phenomenology, as the GC is a highly motile structure that rapidly

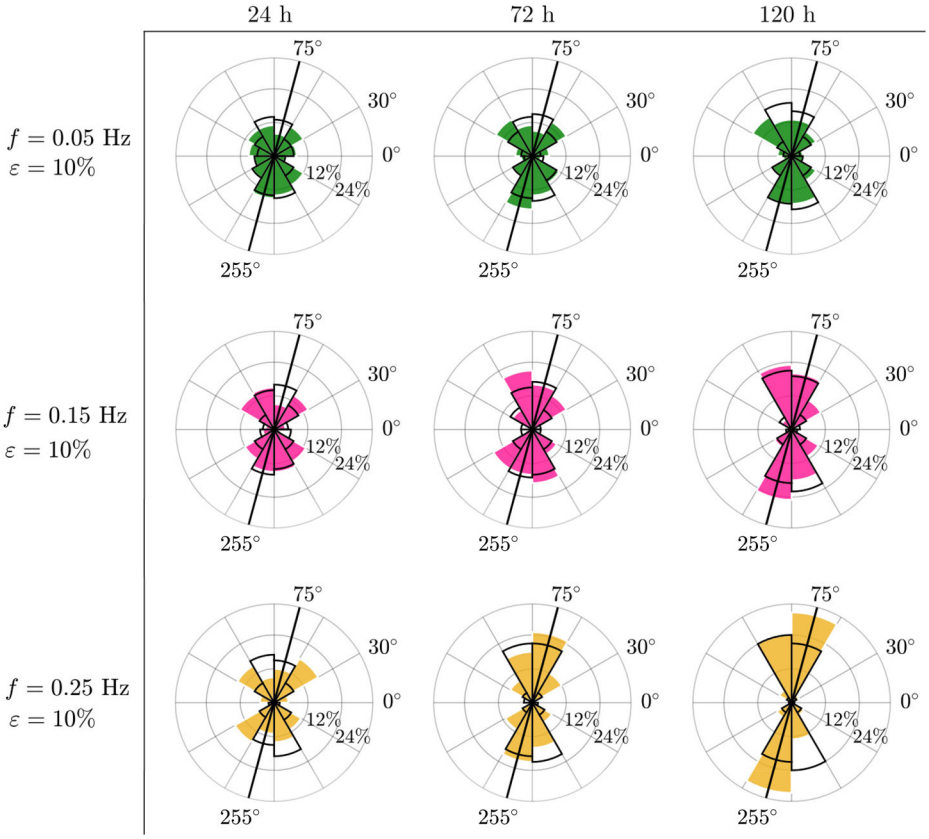


**FIGURE 9** | Simulated neuron reorientation with tubulin-driven axonal growth model and strain amplitude $\varepsilon$ fixed to 10%. Different strain frequencies are considered: $f = 0.05$ Hz (top row), $f = 0.15$ Hz (central row), $f = 0.25$ Hz (bottom row). For each case, 120 neurons initially uniformly distributed over $[0, 2\pi]$ are simulated. Polar histograms show the distribution of their axonal shaft direction $\varphi$ at 24 h (left), 72 h (central), and 120 h (right). In all cases, the circle has been divided into 12 slices measuring 30° each and the percentage of neurons falling into each sector is recorded. As a remark, the equilibrium direction $\theta_{eq} = 75°$ is highlighted. The results of the biological experiments from [20] are shown as black contours to facilitate comparison with the numerical simulations.

changes direction, guiding the axon to alter its growth trajectory. Since in the experimental setting the measured angle corresponds to the axon orientation, in this section, all results refer to $\varphi(t)$. However, once the GC reaches its equilibrium orientation, the axon direction tends to align with it, as can be theoretically proved (see Section B). Thus, in practice, we can compare the time evolution of the axon orientation $\varphi(t)$ reported in Figure 10, with the time evolution of the direction of the GC shown in Figure 5. In all considered cases, the two directions consistently evolve possibly converging to the equilibrium state. Interestingly, the random fluctuation affecting the dynamics of the GC, results less evident in the dynamics of the axon direction $\varphi$.

In addition, to compare the behavior of our model with the experimental results obtained under all combinations of stretching amplitudes and frequencies we evaluate the *order parameter*, defined as

$$\langle \cos 2\hat{\varphi}(t) \rangle = \frac{1}{N} \sum_{i=1}^{N} \cos 2\hat{\varphi}_i(t) \tag{21}$$

where $\hat{\varphi}_i(t) = \arccos(|\cos \varphi_i(t)|)$ with $i = 1, \ldots, N$, denotes the orientation angle of the axonal shaft in the $i$-th model realization. The value of this statistics can span from $-1$ to 1: a random orientation of the sample corresponds to 0, a fully coherent parallel orientation results in 1, and a fully perpendicular orientation corresponds to $-1$. The numerical and experimental results are compared in Figure 11.

The numerical results of our model summarized in the colored regions in the circular histograms in Figures 8 and 9, for different instants of time, are in good agreement with the biological experiments in [20] (black contours).

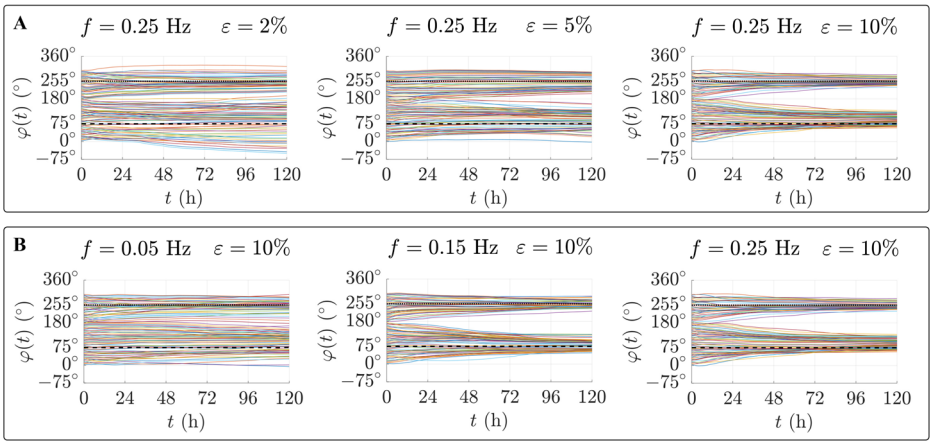


**FIGURE 10** | Time evolution of $\varphi$ of 120 neurons, initially uniformly distributed over $[0, 2\pi]$. (A) Strain frequency $f$ is fixed to 0.25 Hz, while different strain amplitudes are considered: $\varepsilon = 2\%$ (left), $\varepsilon = 5\%$ (central), $\varepsilon = 10\%$ (right). (B) Strain amplitude $\varepsilon$ is fixed to 10%, while different strain frequencies are considered: $f = 0.05$ Hz (left), $f = 0.15$ Hz (central), $f = 0.25$ Hz (right). In all cases, the dashed and dotted line denote the equilibrium configurations $\theta_{eq} = 75°$ and 255°, respectively.

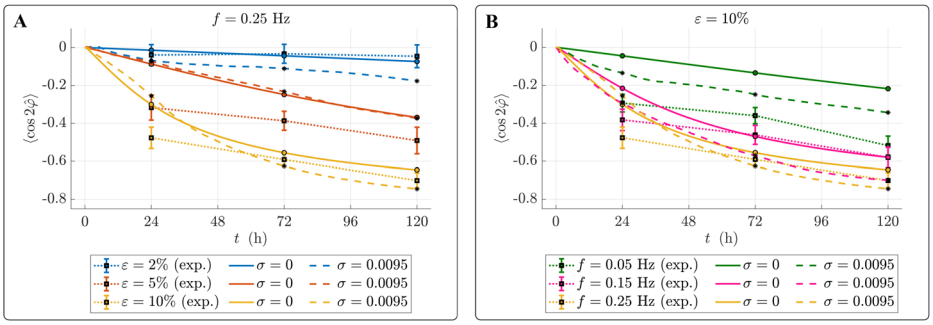


**FIGURE 11** | Evolution of the order parameter obtained by solving the complete model for neuron growth on a substrate subjected to cyclic stretch with different values of amplitude and stretch. (A) Variation of the stretch amplitude with frequency fixed to $f = 0.25$ Hz. (B) Variation of the stretch frequency with amplitude fixed to $\varepsilon = 10\%$. In both cases, the empty circles are experimental data from [20] with error bars representing the standard deviation; solid and dashed curves are the results of the model simulations with $\sigma = 0$ or $\sigma = 0.0095$, respectively.

Furthermore, the results in Figures 8 and 9 demonstrate that our model effectively captures the reorientation process. In particular, the simulations show that neurons tend to preferentially align at angles within the range $[60°, 90°]$ relative to the main stretching direction. This is further corroborated by the monotonically decreasing trend of the computed order parameter, in line with the experimental data, as shown in Figure 11. Additionally, the different behaviors experimentally observed when varying the stretching frequency and amplitude are effectively reproduced. An increase in either the strain amplitude $\varepsilon$ or frequency $f$ substantially accelerates the reorientation process, see Figures 8 and 9 from top to bottom. However, the order parameter values reported in Figure 11A show that a sufficiently high strain amplitude is required to trigger axon reorientation. This indicates that the absence of reorientation biologically observed for small strains is also captured by the model. For instance, in Figure 8, despite the high frequency $f = 0.25$ Hz, the low strain of $\varepsilon = 2\%$ leads to an almost uniform distribution of the neurons' orientation angles even after 120 h of cyclic deformation.

Referring to Figure 11, some limitations of the proposed model can be identified. First, Figure 11B highlights that when using a low frequency $f = 0.05$ Hz the model struggles to produce results that faithfully match the experimental data. This discrepancy is also noticeable when comparing Figure 9 with the experimental counterpart in [20]. Furthermore, although the reorientation process occurs, it is not simulated quickly enough, resulting in a broader angular distribution of the axonal orientations in the numerical simulation compared to the biological data. More generally, Figure 11 shows that at 24 h the reorientation process is underestimated, with numerical order parameters higher than the experimental ones, except for $\varepsilon = 2\%$. At 72 and 120 h, the reorientation process is still underestimated when the stretching amplitude is set to $\varepsilon = 5\%$ (see Figure 11A). With a higher stretching amplitude, i.e., $\varepsilon = 10\%$, low frequencies still result in an underestimation

of axon reorientation, while at higher frequencies the process is accurately captured. In summary, our model quantitatively fits the experimental results either with very small stretching amplitudes or when both stretching amplitude and frequency are sufficiently high.

Discrepancies between the numerical and experimental outcomes detected for intermediate cases may be due to the fact that the numerical order parameter refers to 120 repetitions of a numerical simulation performed by considering an individual neuron always located at the center of the substrate. While the order parameter values reported in [20] have been computed by considering an experiment performed with neurons distributed over the deformed substrate. It should be therefore investigated if some mutual interactions between neurons, possibly mediated by local deformations of the substrate acted by the neurons, affect the orientation process.

## 4 | Conclusion

The directional orientation and growth of axons in response to cyclic stretch remain critical and yet under-explored areas in both biological and modeling perspectives. This study aims to address this gap by developing a novel model for the axonal reorientation and elongation under cyclic mechanical stimuli, focusing on the tip-growth phase. The model integrates a linear viscoelastic reorientation framework, adapted from [32], and a tubulin-driven axonal growth model, taken from [25]. These two frameworks were successfully combined to simulate neuron reorientation in response to different combinations of stretching frequencies and strain amplitudes. Specifically, compared to [32], which focuses on reorientation dynamics in generic cell types, the present model specifically addresses neuronal behavior under cyclic stretch by coupling axonal reorientation and elongation within a unified framework. It further incorporates stochastic fluctuations in directional dynamics to account for GC variability. Finally, we systematically explore how stretch amplitude and frequency affect neuronal alignment and outgrowth, comparing simulation results with experimental observations where available.

Cyclic stretch triggers the reorientation of the GC, which consequently guides axonal growth. The axonal growth is driven by the polymerization of free tubulin, transported from the soma to the GC through a convection–diffusion process. We remark that in the present model, the tubulin-driven growth mechanism is decoupled from the mechanical framework. This choice is motivated by the experimental findings reported in [20], where no significant differences in axonal length were observed between neurons subjected to cyclic mechanical stretch and control samples. As such, a similar growth behavior could be reproduced by simply prescribing an explicit time-dependent growth velocity based on biological data. However, the current formulation offers the advantage of mechanistically linking the GC speed to biologically relevant processes, rather than relying solely on empirical rules. Numerical simulations demonstrated the model's ability to reproduce neuron behaviors observed in experiments, particularly under high-frequency stretching conditions and over long periods. The model effectively mimics the faster reorientation process observed with increasing strain amplitude and frequency.

Validation against experimental observations reported by Lin et al. [20] showed good agreement in most cases, accurately predicting neuron reorientation angles and growth patterns under various stretching conditions. However, some discrepancies were noted at low-frequency values and shorter periods, indicating areas for future model refinement. Specifically, the model has been able to fit the different behaviors between the 0.15 Hz case and the 0.25 Hz one after 72 and 120 h. The model has also been able to mimic the absence of the reorientation when $\varepsilon = 2\%$ and $f = 0.25$ Hz. Conversely, the model lacks in finely reproducing what happens in the experiments when the strain amplitude is equal to 5% and in the case of a relatively low frequency $f = 0.05$ Hz.

Indeed, the current model assumes a linear mechanical behavior of the substrate and is derived under the assumption of small deformation, which may not hold under the stretching conditions of some biological tests. Future work should take into account large deformations and incorporate nonlinearities [31, 53] in substrate mechanical response to improve model accuracy. Additionally, the interaction between the neuron and the substrate, including the traction forces exerted by the GC, should be considered to provide a more realistic representation of neuronal behavior. This involves modeling adhesion formation and detachment processes along the axon and GC. Then, incorporating a tension-dependent term into the axon growth model could account for enhanced growth velocities under cyclic stretch, aligning with observations from other studies [9]. As such, the proposed model provides an extensible framework to investigate hypotheses on how mechanical stress and stretching may influence tubulin dynamics and, consequently, axon elongation. This approach also allows for the future integration of stress-dependent terms into the tubulin-driven growth model, possibly supported by biological evidences. The accurate description of the mechanical interaction between the neuron and the substrate could also help in describing the stretch growth or towed axon phase, not taken into account in the present work. Furthermore, the representation of the neuron's mechanical behavior along the shaft, including its interactions with the substrate,

could help to achieve a realistic description of axon shape, relaxing the assumption of a straight axonal shaft, following approaches such as those proposed by Oliveri and Goriely [27].

From a numerical perspective, adopting a more efficient time discretization scheme than the explicit Euler method used in this study could significantly reduce computing time, allowing for the simulation of longer experimental periods with more neurons. On the other hand, more experimental and mechanical tests are required to properly set the parameters of the proposed model and confirm the parameter estimation done in this work.

In conclusion, this study presents a comprehensive model for neuron reorientation and growth under cyclic stretching, validated against experimental data. The findings underscore the importance of mechanical stimuli in neuronal development and provide a basis for further investigations into the complex interplay between neurons and their mechanical environment.


### Acknowledgments

The authors wish to thank Giulio Lucci and Roberto Marchello for their support in developing the numerical code for the simulations. GC and AC are members of the Gruppo Nazionale di Fisica Matematica, Istituto Nazionale di Alta Matematica (GNFM-INdAM). This work has been supported by the National Plan for Complementary Investments to the NRRP, project "$D^3$4H—Digital Driven Diagnostics, prognostics and therapeutics for sustainable Health care" [project code PNC0000001, CUP B53C22006100001], Spoke 4, funded by Italian Ministry of University and Research, and European Union—NextGeneration EU. AC has been also supported by the Research Project Prin2022 of National Relevance [project code P2022KHFNB, CUP E53D23017990001] granted by Italian Ministry of University and Research, and the European Union—Next Generation EU.

Open access publishing facilitated by Politecnico di Torino, as part of the Wiley - CRUI-CARE agreement.


### Data Availability Statement

Data are available under request.

### References


1. A. Goriely, "Interdisciplinary Applied Mathematics," in *The Mathematics and Mechanics of Biological Growth*, 1st ed., Vol. 45 (Springer-Verlag, 2017).

2. L. A. Lowery and D. V. Vactor, "The Trip of the Tip: Understanding the Growth Cone Machinery," *Nature Reviews Molecular Cell Biology* 10, no. 5 (2009): 332–343, https://doi.org/10.1038/nrm2679.

3. M. O'Toole, P. Lamoureux, and K. E. Miller, "A Physical Model of Axonal Elongation: Force, Viscosity, and Adhesions Govern the Mode of Outgrowth," *Biophysical Journal* 94, no. 7 (2008): 2610–2620, https://doi.org/10.1529/biophysj.107.117424.

4. P. Weiss, "Nerve Patterns: The Mechanics of Nerve Growth," *Third Growth Symposium, Growth (suppl.)* 5 (1941): 163–203.

5. P. Weiss and H. B. Hiscoe, "Experiments on the Mechanism of Nerve Growth," *Journal of Experimental Zoology* 107, no. 3 (1948): 315–395, https://doi.org/10.1002/jez.1401070302.

6. D. Bray, "Axonal Growth in Response to Experimentally Applied Mechanical Tension," *Developmental Biology* 102, no. 2 (1984): 379–389, https://doi.org/10.1016/0012-1606(84)90202-1.

7. T. J. Dennerll, P. Lamoureux, R. E. Buxbaum, and S. R. Heidemann, "The Cytomechanics of Axonal Elongation and Retraction," *Journal of Cell Biology* 109, no. 6 (1989): 3073–3083, https://doi.org/10.1083/jcb.109.6.3073.

8. D. H. Smith, "Stretch Growth of Integrated Axon Tracts: Extremes and Exploitations," *Progress in Neurobiology* 89, no. 3 (2009): 231–239, https://doi.org/10.1016/j.pneurobio.2009.07.006, https://www.sciencedirect.com/science/article/pii/S0301008209001099.

9. P. Lamoureux, R. Buxbaum, and S. Heidemann, "Direct Evidence That Growth Cones Pull," *Nature* 340 (1989): 159–162, https://doi.org/10.1038/340159a0.

10. K. Franze, "Integrating Chemistry and Mechanics: The Forces Driving Axon Growth," *Annual Review of Cell and Developmental Biology* 36, no. 1 (2020): 61–83, https://doi.org/10.1146/annurev-cellbio-100818-125157.

11. P. Recho, A. Jerusalem, and A. Goriely, "Growth, Collapse, and Stalling in a Mechanical Model for Neurite Motility," *Phys. Rev. E* 93 (2016): 032410, https://doi.org/10.1103/PhysRevE.93.032410.

12. K. Miller and D. Suter, "An Integrated Cytoskeletal Model of Neurite Outgrowth," *Frontiers in Cellular Neuroscience* 12 (2018): 447, https://doi.org/10.3389/fncel.2018.00447.

13. H. Oliveri and A. Goriely, "Mathematical Models of Neuronal Growth," *Biomechanics and Modeling in Mechanobiology* 21, no. 1 (2022): 89–118, https://doi.org/10.1007/s10237-021-01539-0.

14. S. Shah, J. Chetta, and B. Bober, "Axonal Transport and Neuromechanics," in *Molecular and Cellular Biomechanics*, ed. B. Layton (Pan Stanford, 2015), 99–126, https://doi.org/10.1201/b18093-7.

15. K. Franze, "The Mechanical Control of Nervous System Development," *Development* 140, no. 15 (2013): 3069–3077, https://doi.org/10.1242/dev.079145.

16. J. Rajagopalan, A. Tofangchi, and M. T. A. Saif, "Drosophila Neurons Actively Regulate Axonal Tension in Vivo," *Biophysical Journal* 99, no. 10 (2010): 3208–3215, https://doi.org/10.1016/j.bpj.2010.09.029.

17. S. Higgins, J. S. Lee, L. Ha, and J. Y. Lim, "Inducing Neurite Outgrowth by Mechanical Cell Stretch," *BioResearch Open Access* 2, no. 3 (2013): 212–216, https://doi.org/10.1089/biores.2013.0008.

18. Y. Ishibashi, K. Uesugi, and K. Morishima, "Effect of Mechanical Stimulation on Neurite Outgrowth of Dorsal Root Ganglion Neurons Toward Integrative Mechanobiologic Nerve Bridge," in *IEEE SICE International Symposium on System Integration (SII)* (Sapporo, Japan, 2016), 797–802, https://doi.org/10.1109/SII.2016.7844097.

19. F. Haq, C. Keith, and G. Zhang, "Neurite Development in PC12 Cells on Flexible Micro-Textured Substrates Under Cyclic Stretch," *Biotechnology Progress* 22, no. 1 (2006): 133–140, https://doi.org/10.1021/bp0501625.

20. J. Lin, X. Li, J. Yin, and J. Qian, "Effect of Cyclic Stretch on Neuron Reorientation and Axon Outgrowth," *Frontiers in Bioengineering and Biotechnology* 8 (2020): 597867, https://doi.org/10.3389/fbioe.2020.597867.

21. C. Giverso, N. Loy, G. Lucci, and L. Preziosi, "Cell Orientation Under Stretch: A Review of Experimental Findings and Mathematical Modelling," *Journal of Theoretical Biology* 572 (2023): 111564, https://doi.org/10.1016/j.jtbi.2023.111564.

22. B. P. Graham and A. Van Ooyen, "Compartmental Models of Growing Neurites," *Neurocomputing* 38–40 (2001): 31–36, https://doi.org/10.1016/S0925-2312(01)00463-5.

23. D. R. McLean and B. P. Graham, "Mathematical Formulation and Analysis of a Continuum Model for Tubulin-Driven Neurite Elongation," *Proceedings of the Royal Society of London. Series A: Mathematical, Physical and Engineering Sciences* 460, no. 2048 (2004): 2437–2456, https://doi.org/10.1098/rspa.2004.1288.

24. B. P. Graham, K. Lauchlan, and D. R. Mclean, "Dynamics of Outgrowth in a Continuum Model of Neurite Elongation," *Journal of Computational Neuroscience* 20, no. 1 (2006): 43–60, https://doi.org/10.1007/s10827-006-5330-3.

25. S. Diehl, E. Henningsson, A. Heyden, and S. Perna, "A One-Dimensional Moving-Boundary Model for Tubulin-Driven Axonal Growth," *Journal of Theoretical Biology* 358 (2014): 194–207, https://doi.org/10.1016/j.jtbi.2014.06.019.

26. S. Diehl, E. Henningsson, and A. Heyden, "Efficient Simulations of Tubulin-Driven Axonal Growth," *Journal of Computational Neuroscience* 41, no. 1 (2016): 45–63, https://doi.org/10.1007/s10827-016-0604-x.

27. H. Oliveri, K. Franze, and A. Goriely, "Theory for Durotactic Axon Guidance," *Physical Review Letters* 126, no. 11 (2021): 118101, https://doi.org/10.1103/PhysRevLett.126.118101.

28. C. Kassianides, A. Goriely, and H. Oliveri, "The Multiscale Mechanics of Axon Durotaxis," *Journal of the Mechanics and Physics of Solids* 200 (2025): 106134, https://doi.org/10.1016/j.jmps.2025.106134, https://www.sciencedirect.com/science/article/pii/S0022509625001103.

29. H. Oliveri, R. De Rooij, E. Kuhl, and A. Goriely, "Rheology of Growing Axons," *Physical Review Research* 4, no. 3 (2022): 033125, https://doi.org/10.1103/PhysRevResearch.4.033125.

30. J. A. García-Grajales, A. Jérusalem, and A. Goriely, "Continuum Mechanical Modeling of Axonal Growth," *Computer Methods in Applied Mechanics and Engineering* 314 (2017): 147–163, Special Issue on Biological Systems Dedicated to William S. Klug, https://doi.org/10.1016/j.cma.2016.07.032.

31. G. Lucci and L. Preziosi, "A Nonlinear Elastic Description of Cell Preferential Orientations Over a Stretched Substrate," *Biomechanics and Modeling in Mechanobiology* 20, no. 2 (2021): 631–649, https://doi.org/10.1007/s10237-020-01406-4.

32. G. Lucci, C. Giverso, and L. Preziosi, "Cell Orientation Under Stretch: Stability of a Linear Viscoelastic Model," *Mathematical Biosciences* 337 (2021): 108630, https://doi.org/10.1016/j.mbs.2021.108630.

33. T. K. Kim, J. K. Kim, and O. C. Jeong, "Measurement of Nonlinear Mechanical Properties of PDMS Elastomer," *Microelectronic Engineering* 88, no. 8 (2011): 1982–1985, https://doi.org/10.1016/j.mee.2010.12.108.

34. F. Johansson, P. Carlberg, N. Danielsen, L. Montelius, and M. Kanje, "Axonal Outgrowth on Nano-Imprinted Patterns," *Biomaterials* 27, no. 8 (2006): 1251–1258, https://doi.org/10.1016/j.biomaterials.2005.07.047.

35. W. Li, Q. Y. Tang, A. D. Jadhav, et al., "Large-Scale Topographical Screen for Investigation of Physical Neural-Guidance Cues," *Scientific Reports* 5, no. 1 (2015): 8644, https://doi.org/10.1038/srep08644.

36. J. P. Sunnerberg, M. Descoteaux, D. L. Kaplan, and C. Staii, "Axonal Growth on Surfaces With Periodic Geometrical Patterns," *PLOS ONE* 16, no. 9 (2021): e0257659, https://doi.org/10.1371/journal.pone.0257659.

37. H. Suo, Z. Wang, G. Dai, J. Fu, J. Yin, and L. Chang, "Polyacrylonitrile Nerve Conduits With Inner Longitudinal Grooved Textures to Enhance Neuron Directional Outgrowth," *Journal of Microelectromechanical Systems* 27, no. 3 (2018): 457–463, https://doi.org/10.1109/JMEMS.2018.2810097.

38. J. M. Vensi Basso, I. Yurchenko, M. Simon, D. J. Rizzo, and C. Staii, "Role of Geometrical Cues in Neuronal Growth," *Physical Review E* 99, no. 2 (2019): 022408, https://doi.org/10.1103/PhysRevE.99.022408.

39. I. Yurchenko, M. Farwell, D. D. Brady, and C. Staii, "Neuronal Growth and Formation of Neuron Networks on Directional Surfaces," *Biomimetics* 6, no. 2 (2021): 41, https://doi.org/10.3390/biomimetics6020041.

40. D. Zhang, H. Suo, J. Qian, J. Yin, J. Fu, and Y. Huang, "Physical Understanding of Axonal Growth Patterns on Grooved Substrates: Groove Ridge Crossing Versus Longitudinal Alignment," *Bio-Design and Manufacturing* 3, no. 4 (2020): 348–360, https://doi.org/10.1007/s42242-020-00089-1.

41. U. Faust, N. Hampe, W. Rubner, et al., "Cyclic Stress at mhz Frequencies Aligns Fibroblasts in Direction of Zero Strain," *PLoS ONE* 6, no. 12 (2011): e28963, https://doi.org/10.1371/journal.pone.0028963.

42. A. Livne, E. Bouchbinder, and B. Geiger, "Cell Reorientation Under Cyclic Stretching," *Nature Communications* 5, no. 1 (2014): 3938, https://doi.org/10.1038/ncomms4938.

43. J. H. Wang, "Substrate Deformation Determines Actin Cytoskeleton Reorganization: A Mathematical Modeling and Experimental Study," *Journal of Theoretical Biology* 202, no. 1 (2000): 33–41, https://doi.org/10.1006/jtbi.1999.1035.

44. A. Müller, M. C. Wapler, and U. Wallrabe, "A Quick and Accurate Method to Determine The Poisson's Ratio and the Coefficient of Thermal Expansion of PDMS," *Soft Matter* 15, no. 4 (2019): 779–784, https://doi.org/10.1039/C8SM02105H.

45. I. D. Johnston, D. K. McCluskey, C. K. L. Tan, and M. C. Tracey, "Mechanical Characterization of Bulk Sylgard 184 for Microfluidics and Microengineering," *Journal of Micromechanics and Microengineering* 24, no. 3 (2014): 035017, https://doi.org/10.1088/0960-1317/24/3/035017.

46. A. Tamada, S. Kawase, F. Murakami, and H. Kamiguchi, "Autonomous Right-Screw Rotation of Growth Cone Filopodia Drives Neurite Turning," *Journal of Cell Biology* 188, no. 3 (2010): 429–441, https://doi.org/10.1083/jcb.200906043.

47. T. Betz, D. Koch, D. Lim, and J. A. Käs, "Stochastic Actin Polymerization and Steady Retrograde Flow Determine Growth Cone Advancement," *Biophysical Journal* 96, no. 12 (2009): 5130–5138, https://doi.org/10.1016/j.bpj.2009.03.045.

48. N. Loy and L. Preziosi, "A Statistical Mechanics Approach to Describe Cell Reorientation Under Stretch," *Bulletin of Mathematical Biology* 85, no. 60 (2023), https://doi.org/10.1007/s11538-023-01161-4.

49. P. W. Baas, C. Vidya Nadar, and K. A. Myers, "Axonal Transport of Microtubules: The Long and Short of it," *Traffic* 7, no. 5 (2006): 490–498, https://doi.org/10.1111/j.1600-0854.2006.00392.x.

50. M. Caplow and L. Fee, "Dissociation of the Tubulin Dimer is Extremely Slow, Thermodynamically Very Unfavorable, and Reversible in the Absence of an Energy Source," *Molecular Biology of the Cell* 13, no. 6 (2002): 2120–2131, https://doi.org/10.1091/mbc.e01-10-0089.

51. C. H. Keith, "Slow Transport of Tubulin in the Neurites of Differentiated pc12 Cells," *Science, New Series* 235, no. 4786 (1987): 337–339, https://doi.org/10.1126/science.2432662.

52. J. T. Kevenaar and C. C. Hoogenraad, "The Axonal Cytoskeleton: From Organization To Function," *Frontiers in Molecular Neuroscience* 8 (2015): 44, https://doi.org/10.3389/fnmol.2015.00044.

53. J. Merodio and R. Ogden, "The Influence of the Invariant on the Stress–Deformation and Ellipticity Characteristics of Doubly Fiber-Reinforced Non-Linearly Elastic Solids," *International Journal of Non-Linear Mechanics* 41, no. 4 (2006): 556–563, https://doi.org/10.1016/j.ijnonlinmec.2006.02.001.

## Appendix A: Energy Minimization and Equilibrium Orientations

In the present model, the growth cone orientation is driven by the minimization of a general elastic energy density, said $\mathcal{U}$. Indeed, it can be proven [32] that in both high- and low-frequency regime, the deterministic part of Equation (5) reduces to

$$\frac{d\theta(t)}{dt} \propto -\frac{\partial \mathcal{U}}{\partial \theta} = \frac{\partial \mathbb{T}}{\partial \theta} : \mathbb{E}. \tag{A1}$$

In the range of strain amplitudes tested in [20], PDMS has been proven to have a linear elastic behavior [33]. Hence, we hereafter work in the linear approximation by considering just the linear terms of the deformation characterized by the strain tensor $\mathbb{E}$. For this reason, the elastic energy density for the growth cone assumes the following generic form:

$$\mathcal{U} = \mathcal{U}_{\text{iso}}(I_1) + \mathcal{U}_{\text{ortho}}(I_4) + \mathcal{U}_{\text{mix}}(I_1, I_4), \tag{A2}$$

where $\mathcal{U}_{\text{iso}}$ is the purely isotropic contribution, $\mathcal{U}_{\text{ortho}}$ represents the orthotropic contribution, while $\mathcal{U}_{\text{mix}}$ gives the coupling effects of isotropy and anisotropy. In the linear approximation, all the invariants that give higher-order terms are neglected. Hence, all the terms in Equation (A2) depend just on the invariants of $\mathbb{E}$ that give linear terms, i.e.,

$$I_1 := \text{tr}\mathbb{E}, \qquad I_4 := \mathbf{N} \cdot \mathbb{E}\mathbf{N}, \tag{A3}$$

Since the first invariant does not depend on the orientation $\theta$, as $\frac{\partial \mathcal{U}_{\text{iso}}}{\partial \theta} = 0$ the term $\mathcal{U}_{\text{iso}}$ can be neglected in our discussion. Then, the final form of the elastic energy will be

$$\begin{aligned} \mathcal{U} &= \mathcal{U}_{\text{ortho}}(I_4) + \mathcal{U}_{\text{mix}}(I_1, I_4) \\ &= \frac{1}{2}K_{\parallel}(\mathbf{N}\cdot\mathbb{E}\mathbf{N})^2 + 2K_{14}(\text{tr}\,\mathbb{E})(\mathbf{N}\cdot\mathbb{E}\mathbf{N}), \end{aligned} \tag{A4}$$

where $K_{\parallel}$ is a coefficient related to the stiffness along the SFs direction and $K_{14}$ weights the coupling term. We remark that, by working under the small deformations limit, Equation (A4) may be valid also for nonlinear substrates, as shown in [31, 32].

Recalling the explicit forms of $\mathbb{E}$ and $\mathbf{N}$, Equation (A4) becomes

$$\begin{aligned} \mathcal{U} = &\frac{1}{2}K_{\parallel}(\varepsilon_x \cos^2\theta + \varepsilon_y \sin^2\theta)^2 \\ &+ 2K_{14}(\varepsilon_x + \varepsilon_y)(\varepsilon_x \cos^2\theta + \varepsilon_y \sin^2\theta). \end{aligned} \tag{A5}$$

The derivative of $\mathcal{U}$ with respect to the orientation angle is

$$\begin{aligned} \frac{\partial \mathcal{U}}{\partial \theta} = &2K_{\parallel}\sin\theta\cos\theta(\varepsilon_y - \varepsilon_x)(\varepsilon_x \cos^2\theta + \varepsilon_y \sin^2\theta) \\ &+ 4K_{14}(\varepsilon_x + \varepsilon_y)(\varepsilon_y - \varepsilon_x)\sin\theta\cos\theta \end{aligned} \tag{A6}$$

and the equilibrium condition $\frac{\partial \mathcal{U}}{\partial \theta} = 0$ reads

$$2(\varepsilon_y - \varepsilon_x)\cos\theta\sin\theta\left[K_{\parallel}\varepsilon_x\cos^2\theta + K_{\parallel}\varepsilon_y\sin^2\theta + 2K_{14}(\varepsilon_x + \varepsilon_y)\right] = 0. \tag{A7}$$

Considering the interval $[0, \pi]$, Equation (A7) is satisfied under one of the following conditions on the interval:

- $\sin\theta = 0 \quad \Rightarrow \quad \theta_{\text{eq}} = 0, \pi$,
- $\cos\theta = 0 \quad \Rightarrow \quad \theta_{\text{eq}} = \frac{\pi}{2}$,
- $\cos^2\theta_{\text{eq}} = \frac{2K_{14}(\varepsilon_x + \varepsilon_y) + K_{\parallel}\varepsilon_y}{K_{\parallel}(\varepsilon_y - \varepsilon_x)}$.

The first condition defines the *parallel* equilibrium orientation, the second gives the *perpendicular* orientation, whereas the third condition leads to the definition of the so called *oblique equilibrium*. By substituting the relation $\varepsilon_y = -r\varepsilon_x$, the oblique equilibrium should satisfy

$$\cos^2\theta_{\text{eq}} = \frac{1}{2} + \mathcal{K}\left(\frac{1}{2} - \frac{1}{r+1}\right) = \frac{1}{2}\left(1 - \mathcal{K}\,\frac{1-r}{1+r}\right) \tag{A8}$$

where we have introduced the parameter

$$\mathcal{K} = \frac{K_{\parallel} + 4K_{14}}{K_{\parallel}} = 1 + 4\frac{K_{14}}{K_{\parallel}} \tag{A9}$$

that embodies all the mechanical characteristics of the growth cone-substratum media. This is consistent with the results presented in [31, 32, 42]. From Equation (A8), it is clear that the parameter $r$ is fundamental to determine the final equilibrium angle of the growth cone. This parameter is easily tunable in biaxial experiments and controlled by imposing different deformations to the substratum or by using different clamps for stretching it. A complete study on the incidence of $r$ on the cell orientation angle is made in [42], even if the study has not been conducted on neuron-type cells.

We here focus on the stability of the equilibrium angles, taking $\mathcal{K} > 1$. Indeed, thanks to Equation (A9), this case holds always true in our specific case. Let us first introduce the parameter $\rho := \frac{\mathcal{K}+1}{\mathcal{K}-1}$ and set the conditions of existence for the oblique equilibrium. Of course, since

$$0 \le \cos^2\theta_{\text{eq}} \le 1 \tag{A10}$$

the oblique equilibrium angle exists if $\frac{1}{\rho} < r < \rho$. The parallel and perpendicular angles, instead, always exist.

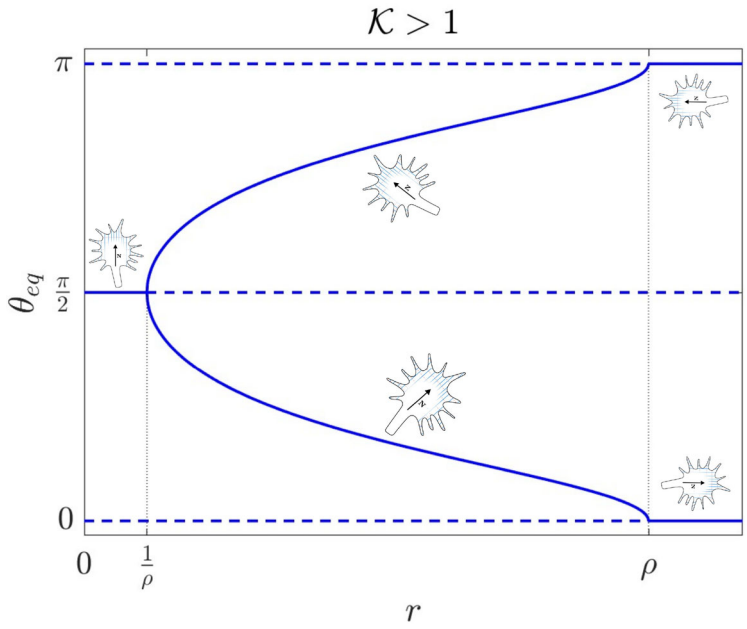


**FIGURE A1** | Bifurcation diagram for the case $\mathcal{K} > 1$. The solid line represents the stable equilibrium while the dashed ones are the unstable equilibrium.

In order to conduct the stability study, we write down the second-order derivative of our energy $\mathcal{U}$ with respect to $\theta$

$$\frac{\partial^2 \mathcal{U}}{\partial \theta^2} = 2\varepsilon_x^2(r+1)\left[K_{\parallel}\cos^2\theta(1+r) + 2K_{14}(1-r) - K_{\parallel}r\right]\left(\cos^2\theta - \sin^2\theta\right) + 4\varepsilon_x^2(r+1)^2 K_{\parallel}\cos^2\theta\sin^2\theta \tag{A11}$$

and set the general stability condition as follows:

$$\left.\frac{\partial^2 \mathcal{U}}{\partial \theta^2}\right|_{\theta=\theta_{\text{eq}}} > 0. \tag{A12}$$

Considering $\mathcal{K} > 1$, the stability analysis gives the following results (reported also in Figure A1):

- $\theta_{\text{eq}} = 0$ is stable if $r > \rho$;
- $\theta_{\text{eq}} = \frac{\pi}{2}$ is stable if $r < \frac{1}{\rho}$;
- the oblique equilibrium angles are always stable.

## Appendix B: Growth Cone and Axon Orientations

In the proposed model, the orientation angle of the growth cone, $\theta(t)$, and the orientation of the axon, $\varphi(t)$, see Figure 2, may generally differ. However, once the growth cone reaches its equilibrium orientation, the axon direction tends to align with it, as stated in the following theorem.

**Theorem A1.** *If the growth cone reaches an equilibrium direction $\theta_{eq}$, for a time that is large enough, the following equality holds*

$$\varphi_{eq} := \lim_{t\to\infty} \varphi(t) = \theta_{eq}. \tag{B1}$$

*Proof.* We refer to Figure B1 where we set as $\mathbf{X}_S$ and $\mathbf{X}_{\text{GC}}$ the soma and the growth cone position, respectively. The point $P$ is the spot where the GC reaches the equilibrium orientation $\theta_{\text{eq}}$. Hereafter, the growth cone moves along the straight line $b$ and its orientation does not change because it has reached the equilibrium value. Referring to Figure B1, we define the angle $\beta$ as the difference between the GC equilibrium angle and the axon direction:

$$\beta(t) := \theta_{\text{eq}} - \varphi(t). \tag{B2}$$

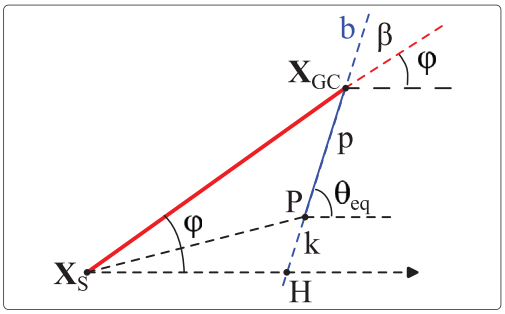


**FIGURE B1** | Representation of the condition stated in Equation (B1).

We consider the triangle $\mathbf{X}_S\hat{H}\mathbf{X}_{GC}$ and define $p = \overline{P\mathbf{X}_{GC}}$, $k = \overline{HP}$ and $u = \overline{\mathbf{X}_S H}$. We then apply the law of sines to get

$$\frac{\sin\varphi}{p+k} = \frac{\sin\beta}{u} \qquad \Rightarrow \qquad \sin\beta = \frac{u}{p+k}\sin\varphi. \tag{B3}$$

We can now write

$$\sin\varphi = \sin\left(\theta_{eq} - \beta\right) = \sin\theta_{eq}\cos\beta - \sin\beta\cos\theta_{eq} \tag{B4}$$

and by substituting Equation (B3) in the previous equality, we get

$$\sin\beta\left[1 + \frac{u}{p+k}\cos\theta_{eq}\right] = \frac{u}{p+k}\sin\theta_{eq}\cos\beta \tag{B5}$$

that finally leads to

$$\tan\beta = \frac{\sin\theta_{eq}}{\frac{p+k}{u} + \cos\theta_{eq}}. \tag{B6}$$

For sufficiently large times ($t \to \infty$), the axon continues to grow leading the distance $p \to \infty$. Thus, the term $\tan\beta \to 0$ and consequently $\beta \to 0$. We finally obtain the following asymptotic result:

$$\lim_{t\to\infty}\beta(t) = \lim_{t\to\infty}\left(\theta_{eq} - \varphi(t)\right) = 0. \tag{B7}$$

Thus, defining $\varphi_{eq} := \lim_{t\to\infty}\varphi(t)$ we have Equation (B1). □